The Astronomical Journal, 166:90 (22pp), 2023 September https://doi.org/10.3847/1538-3881/ace1ef

The Unusual M-dwarf Warm Jupiter TOI-1899 b: Refinement of Orbital and Planetary Parameters

Andrea S. J. Lin[1,2], Jessica E. Libby-Roberts[1,2], Jaime A. Alvarado-Montes[3,4], Caleb I. Cañas[1,2,5,31], Shubham Kanodia[6], Te Han[7], Leslie Hebb[8,9], Eric L. N. Jensen[10], Suvrath Mahadevan[1,2,11], Luke C. Powers[1], Tera N. Swaby[12], John Wisniewski[13], Corey Beard[7], Chad F. Bender[14], Cullen H. Blake[15], William D. Cochran[16], Scott A. Diddams[17,18,19], Robert C. Frazier[1,2], Connor Fredrick[18,19], Michael Gully-Santiago[20], Samuel Halverson[21], Sarah E. Logsdon[22], Michael W. McElwain[23], Caroline Morley[20], Joe P. Ninan[24], Jayadev Rajagopal[22], Lawrence W. Ramsey[1,2], Paul Robertson[7], Arpita Roy[25,26], Christian Schwab[3], Guðmundur Stefánsson[27,32], Daniel J. Stevens[28], Ryan C. Terrien[29], and Jason T. Wright[1,2,30]

[1] Department of Astronomy & Astrophysics, 525 Davey Laboratory, The Pennsylvania State University, University Park, PA 16802, USA; asjlin@psu.edu
[2] Center for Exoplanets and Habitable Worlds, 525 Davey Laboratory, The Pennsylvania State University, University Park, PA 16802, USA
[3] School of Mathematical and Physical Sciences, Macquarie University, Balaclava Road, North Ryde, NSW 2109, Australia
[4] The Macquarie University Astrophysics and Space Technologies Research Centre, Macquarie University, Balaclava Road, North Ryde, NSW 2109, Australia
[5] NASA Goddard Space Flight Center, 8800 Greenbelt Road, Greenbelt, MD 20771, USA
[6] Earth and Planets Laboratory, Carnegie Institution for Science, 5241 Broad Branch Road NW, Washington, DC 20015, USA
[7] Department of Physics & Astronomy, The University of California, Irvine, CA 92697, USA
[8] Physics Department, Hobart and William Smith Colleges, 300 Pulteney Street, Geneva, NY 14456, USA
[9] Department of Astronomy, Cornell University, 245 East Avenue, Ithaca, NY 14850, USA
[10] Department of Physics & Astronomy, Swarthmore College, Swarthmore, PA 19081, USA
[11] ETH Zurich, Institute for Particle Physics & Astrophysics, Zurich, Switzerland
[12] Department of Physics & Astronomy, University of Wyoming, 1000 E. University, Dept. 3905, Laramie, WY 82071, USA
[13] NASA Headquarters, 300 Hidden Figures Way SW, Washington, DC 20546, USA
[14] Steward Observatory, University of Arizona, 933 N. Cherry Avenue, Tucson, AZ 85721, USA
[15] Department of Physics and Astronomy, University of Pennsylvania, 209 South 33rd Street, Philadelphia, PA 19104, USA
[16] McDonald Observatory and Center for Planetary Systems Habitability, The University of Texas, Austin, TX 78712, USA
[17] Electrical, Computer & Energy Engineering, 425 UCB, University of Colorado, Boulder, CO 80309, USA
[18] Department of Physics, 390 UCB, University of Colorado, Boulder, CO 80309, USA
[19] National Institute of Standards & Technology, 325 Broadway, Boulder, CO 80305, USA
[20] Department of Astronomy, The University of Texas at Austin, Austin, TX 78712, USA
[21] Jet Propulsion Laboratory, 4800 Oak Grove Drive, Pasadena, CA 91109, USA
[22] NSF's National Optical-Infrared Astronomy Research Laboratory, 950 N. Cherry Avenue, Tucson, AZ 85719, USA
[23] Exoplanets and Stellar Astrophysics Laboratory, NASA Goddard Space Flight Center, Greenbelt, MD 20771, USA
[24] Department of Astronomy and Astrophysics, Tata Institute of Fundamental Research, Homi Bhabha Road, Colaba, Mumbai 400005, India
[25] Space Telescope Science Institute, 3700 San Martin Drive, Baltimore, MD 21218, USA
[26] Department of Physics and Astronomy, Johns Hopkins University, 3400 N. Charles Street., Baltimore, MD 21218, USA
[27] Department of Astrophysical Sciences, Princeton University, 4 Ivy Lane, Princeton, NJ 08540, USA
[28] Department of Physics & Astronomy, University of Minnesota Duluth, Duluth, MN 55812, USA
[29] Carleton College, One North College Street, Northfield, MN 55057, USA
[30] Penn State Extraterrestrial Intelligence Center, 525 Davey Laboratory, The Pennsylvania State University, University Park, PA 16802, USA
Received 2023 January 25; revised 2023 June 2; accepted 2023 June 16; published 2023 August 3

Abstract

TOI-1899 b is a rare exoplanet, a temperate warm Jupiter orbiting an M dwarf, first discovered by Cañas et al. (2020) from a TESS single-transit event. Using new radial velocities (RVs) from the precision RV spectrographs HPF and NEID, along with additional TESS photometry and ground-based transit follow-up, we are able to derive a much more precise orbital period of $P = 29.090312^{+0.000036}_{-0.000035}$ days, along with a radius of $R_p = 0.99 \pm 0.03\ R_J$. We have also improved the constraints on planet mass, $M_p = 0.67 \pm 0.04\ M_J$, and eccentricity, which is consistent with a circular orbit at 2σ ($e = 0.044^{+0.029}_{-0.027}$). TOI-1899 b occupies a unique region of parameter space as the coolest known ($T_{eq} \approx$ 380 K) Jovian-sized transiting planet around an M dwarf; we show that it has great potential to provide clues regarding the formation and migration mechanisms of these rare gas giants through transmission spectroscopy with JWST, as well as studies of tidal evolution.

Unified Astronomy Thesaurus concepts: Radial velocity (1332); Transit photometry (1709); Extrasolar gaseous planets (2172)

Supporting material: machine-readable table, data behind figures

1. Introduction

The vast majority of planets discovered around M dwarfs are small, with gas giants ($R_p > 8\ R_\oplus$) being rare despite being easier to detect through either transit photometry or radial velocities (RVs). It is relatively easy to explain why such gas giants are thought to be intrinsically rare—both models (e.g.,

[31] NASA Postdoctoral Fellow.
[32] NASA Sagan Fellow.

Laughlin et al. 2004) and observations (e.g., Andrews et al. 2013) indicate that M-dwarf protoplanetary disks are much smaller and less massive than disks around more massive FGK stars. With less gas and dust available, M-dwarf disks should be much less likely to form gas giants (Burn et al. 2021), especially via the core-accretion pathway (Ida & Lin 2004) because the timescale for formation of giant cores is too long relative to the disk lifetime. However, it remains unclear why some M-dwarf disks are capable of forming these giant planets, though M-dwarf gas giants seem to form preferentially around metal-rich stars (Maldonado et al. 2020; Gan et al. 2022), which may host more massive disks with large enough quantities of solids for massive planetary cores to form.

With the recent abundance of space-based photometric data from the Transiting Exoplanet Survey Satellite (TESS; Ricker et al. 2014), we are beginning to find more examples of these rare M-dwarf gas giants, including nine short-period Jupiters ($P \leqslant 10$ days; see Cañas et al. 2022; Gan et al. 2022, and references therein). However, warm Jupiters (WJs)—here defined as gas giant planets with periods between 10 and 100 days—around M dwarfs are much rarer, with only three other examples known apart from TOI-1899 b: the two statistically validated planets Kepler-1628 b ($P = 76.4$ days, $R_p = 6.5\,R_\oplus$; Morton et al. 2016) and K2-387 b ($P = 28.7$ days, $R_p = 7.3\,R_\oplus$; Christiansen et al. 2022), and the very young TOI-1227 b ($P = 27.4$ days, $R_p = 9.6\,R_\oplus$; Mann et al. 2022), which is expected to contract to $\lesssim 5\,R_\oplus$ as it cools. However, TOI-1899 b is the only M-dwarf WJ with a mass measurement. WJs are challenging to discover in TESS photometry, as their longer periods often mean that they are detected only as single-transit events. Even with precision RV follow-up, having only a single transit means that it is often difficult to obtain an ephemeris precise enough to schedule future transit observations (e.g., for transmission spectroscopy). Being able to do so often relies on TESS revisiting the field in later sectors, or extensive reconnaissance observations with ground-based photometry.

WJs around FGK stars largely exhibit low to moderate eccentricities, with the few with high eccentricities thought to be "passing through" on their way to circularize as Hot Jupiters, or possibly excited by companion-induced eccentricity cycling (Dawson & Johnson 2018). Many low-eccentricity WJs also host smaller inner companions (e.g., Weiss et al. 2013; Tran et al. 2022), with Huang et al. (2016) suggesting that the companion fraction is ∼50%. In turn, the high companion fraction indicates that a large fraction of FGK WJs must form through relatively peaceful, dynamically cool mechanisms, e.g., forming in situ or undergoing disk migration. However, since very few M-dwarf WJs are known, it is unknown whether they form in the same ways and at the same rates as their FGK cousins, or whether the small size and low mass of M-dwarf disks compel different formation and evolutionary pathways.

The M-dwarf WJ TOI-1899 b was discovered from a TESS single-transit event (with two sectors of coverage, Sectors 14 and 15) by Cañas et al. (2020), who constrained its orbital period with 15 RVs obtained with the near-infrared (NIR) Habitable-zone Planet Finder spectrograph (HPF; Mahadevan et al. 2012, 2014). In this paper, we update the parameters and orbital elements of this system, using additional RVs from HPF and NEID, three more TESS transits, and ground-based transit photometry.

Section 2 describes our RV and photometric observations and data processing, and Section 3 details what these data tell us about stellar parameters, including activity levels and rotation period. Section 4 presents the updated parameters of the TOI-1899 system. In Section 5, we detail how TOI-1899 b occupies a unique region of parameter space, which makes it a scientifically interesting target both for further atmospheric characterization with JWST and for tidal evolution simulations.

2. Observations

2.1. HPF RVs

HPF is a fiber-fed (Kanodia et al. 2018), high-resolution ($R \sim 50{,}000$), NIR (808–1278 nm) spectrograph. It is thermally stabilized at the millikelvin level (Stefansson et al. 2016) and has demonstrated an on-sky RV precision of $1.53\,\mathrm{m\,s^{-1}}$ (Metcalf et al. 2019). HPF is located at the 10 m Hobby-Eberly Telescope (HET; Ramsey et al. 1998; Hill et al. 2021) at McDonald Observatory, which is a fixed-altitude telescope with a roving pupil design, and is fully queue scheduled with all observations executed in a queue by the HET resident astronomers (Shetrone et al. 2007).

TOI-1899 b was originally published by Cañas et al. (2020) with 15 RVs from HPF. Since then, we have obtained 35 more HPF visits, with each visit comprising two 945 s exposures. We discard six visits which have signal-to-noise ratios (S/Ns) less than half the median S/N per pixel of 57 (measured at 1000 nm). The remaining 29 visits are shown in Table 1. HPF engineering work in 2022 May required thermal and vacuum cycling of the instrument, resulting in an RV offset once HPF had restabilized; we fit separately the RVs taken before and after the velocity break. The phase-folded RVs of TOI-1899 are shown in the top panel of Figure 1.

HPF is capable of simultaneous calibration using an NIR Laser Frequency Comb (LFC; Metcalf et al. 2019), but we chose not to use simultaneous calibration owing to the faintness of our target, in order to minimize the impact of scattered light in the science spectrum. Instead, we obtain a wavelength solution by interpolating the wavelength solution from other LFC exposures on the night of the observations, which has been shown to enable wavelength calibration and drift correction at a precision of $\sim 30\ \mathrm{cm\,s^{-1}}$ (Stefansson et al. 2020), a value much smaller than our estimated per-observation RV uncertainty (instrumental precision and photon noise, added in quadrature) of $\sim 15\ \mathrm{m\,s^{-1}}$ on this target.

We use `HxRGproc` (Ninan et al. 2018) for correction of the raw HPF data and then derive RVs via the methodology outlined in Metcalf et al. (2019). We use a modified version of the `SpEctrum Radial Velocity AnaLyser` (`SERVAL`; Zechmeister et al. 2018) as discussed further in Stefansson et al. (2020), which employs the template-matching technique to derive RVs (e.g., Anglada-Escudé & Butler 2012). We generated the master template using all observed spectra, ignoring telluric regions identified by using a synthetic telluric-line mask generated from `telfit` (Gullikson et al. 2014), a Python wrapper to the Line-by-Line Radiative Transfer Model package (Clough et al. 2005). We calculated the barycentric correction for each epoch using `barycorrpy` (Kanodia & Wright 2018), the Python implementation of the algorithms from Wright & Eastman (2014).

2.2. NEID RVs

NEID (Halverson et al. 2016; Schwab et al. 2016) is an ultrastabilized (Robertson et al. 2019), high-resolution ($R \sim$

110,000) spectrograph mounted on the WIYN 3.5 m Telescope[33] at Kitt Peak National Observatory. NEID is fiber fed via a dedicated port adapter on the WIYN 3.5 m (Logsdon et al. 2018; Schwab et al. 2018) and covers a broad red–optical wavelength range from 380 to 930 nm. It is wavelength calibrated by an astro-comb (a purpose-built LFC) and a Fabry–Pérot etalon. Like HPF, NEID is also capable of simultaneous calibration (using the etalon instead of the LFC), but again we chose not to use this feature owing to the faintness of our target.

We also obtained four visits of TOI-1899 with NEID in HR (High Resolution) mode, with single exposures of 1800 s per visit. Of our four visits, two exhibit significantly lower S/N as a result of poor observing conditions, but we include them anyway owing to the small number of NEID RVs. These are shown in Table 1 and the top panel of Figure 1.

NEID data are automatically reduced by the NEID Data Reduction (https://neid.ipac.caltech.edu/docs/NEID-DRP/). We retrieve the Level-2 (fully processed) 1D spectra from the NEID Data Archive (https://neid.ipac.caltech.edu/search.php) and use a NEID-adapted version of `SERVAL` (Stefánsson et al. 2022) to derive the final RVs. These RVs are calculated from 44 orders centered between 5070 and 8900 Å (order indices 52–104, corresponding to echelle orders 121–69) using only the central-most 3000 pixels of each order, which has been found to result in better RV precision for faint M dwarfs like this one, by using only the highest-S/N portions of the spectra (see, e.g., Cañas et al. 2022).

2.3. TESS Photometry

TESS first observed TOI-1899 during Sectors 14 (2019 July 18–2019 August 14) and 15 (2019 August 15–2019 September 10) at 2-minute cadence, revealing a single-transit event, which was used by Cañas et al. (2020) to derive the initial orbit of this planet. Since then, TESS has reobserved TOI-1899 during Sectors 41 (2021 July 23–2021 August 20), 54 (2022 July 9–2022 August 4), and 55 (2022 August 5–2022 September 1), all at 2-minute cadence. Three more transits were detected during these sectors, allowing us to constrain the planet period much more precisely. We show the TESS transits phase folded in the top left panel of Figure 2. In our analysis, we use the Pre-search Data-Conditioned Simple Aperture Photometry (PDCSAP; Jenkins et al. 2016) light curves available from MAST,[34] which have already been corrected for dilution. However, in our joint fit, we let the TESS dilution float—see Section 4 for details.

2.4. Ground-based Photometry

In our efforts to better characterize the orbit of TOI-1899 b, we made several attempts at observing a ground-based transit of the planet, using the single-transit ephemeris from Cañas et al. (2020). We monitored TOI-1899 with the 0.6 m telescope at Red Buttes Observatory (RBO; Kasper et al. 2016) every night from 2021 June 11 through June 17, but we did not see a transit on any of these nights.[35] It was not until a second TESS transit was detected in Sector 41 that we were able to constrain the planet period well enough for successful ground-based transit photometry; we detail the three successful observations below.

Table 1
RVs of TOI-1899

BJD_{TDB}	RV (m s^{-1})	σ (m s^{-1})	S/N[a]	Instrument[b]
2,458,763.68342	52.68	43.54	34	HPFpre[c]
2,458,778.65399	−23.56	14.51	68	HPFpre
2,458,782.63085	−10.48	12.82	75	HPFpre
2,458,784.63162	16.50	12.63	77	HPFpre
2,458,789.62112	68.47	13.83	71	HPFpre
2,458,793.60354	60.85	21.72	47	HPFpre
2,458,802.58906	−1.13	19.94	50	HPFpre
2,458,803.57261	−46.29	16.95	59	HPFpre
2,458,805.58078	4.14	14.73	67	HPFpre
2,458,809.56162	−14.05	14.30	68	HPFpre
2,458,810.55741	2.57	24.09	42	HPFpre
2,458,811.55496	−7.49	11.77	83	HPFpre
2,458,818.55514	97.10	30.01	36	HPFpre
2,458,819.54226	113.14	15.21	67	HPFpre
2,458,820.54718	102.72	15.44	64	HPFpre
2,458,971.88328	67.59	30.63	34	HPFpre
2,458,974.88034	24.97	29.68	35	HPFpre
2,458,977.88244	−3.99	26.67	38	HPFpre
2,459,004.80488	−22.52	24.76	41	HPFpre
2,459,005.79603	0.05	21.99	45	HPFpre
2,459,006.79804	−17.51	18.45	53	HPFpre
2,459,041.93039	−27.15	16.61	58	HPFpre
2,459,043.70033	−26.60	13.71	71	HPFpre
2,459,057.88720	42.62	14.87	66	HPFpre
2,459,089.80308	20.95	16.62	60	HPFpre
2,459,120.72756	22.37	13.80	72	HPFpre
2,459,125.70312	−42.30	13.50	73	HPFpre
2,459,129.69317	−29.26	13.62	72	HPFpre
2,459,136.67793	61.82	12.86	76	HPFpre
2,459,163.59938	−0.52	18.64	53	HPFpre
2,459,169.57385	51.91	17.52	57	HPFpre
2,459,296.99568	−68.24	24.51	42	HPFpre
2,459,300.99395	−43.55	17.76	55	HPFpre
2,459,382.77297	−16.71	20.60	49	HPFpre
2,459,472.74724	−21.35	18.15	55	HPFpre
2,459,480.72502	21.16	21.48	50	HPFpre
2,459,486.71612	85.63	15.79	64	HPFpre
2,459,492.69426	114.13	17.94	57	HPFpre
2,459,493.69425	76.29	15.50	65	HPFpre
2,459,504.68897	−74.44	7.71	16	NEID
2,459,530.59402	−9.95	17.22	58	HPFpre
2,459,532.67008	−37.32	7.08	17	NEID
2,459,698.89831	16.71	14.02	9	NEID
2,459,714.81917	−11.16	15.39	9	NEID
2,459,715.86110	6.71	17.15	59	HPFpre
2,459,717.84933	89.17	35.15	34	HPFpre
2,459,781.91055	−10.38	19.07	51	HPFpost
2,459,788.89371	−40.33	18.69	52	HPFpost

Notes. Data above the horizontal line were first published in Cañas et al. (2020); data below are presented for the first time in this work.
[a] HPF S/N measured in order index 18 (∼1000 nm), NEID S/N in order index 102 (∼850 nm).
[b] "HPFpre" and "HPFpost" indicate data taken before and after the HPF engineering velocity break, respectively.
[c] Exposure time of 945 s.

(This table is available in machine-readable form.)

[33] The WIYN Observatory is a joint facility of the NSF's National Optical-Infrared Astronomy Research Laboratory, Indiana University, the University of Wisconsin–Madison, Pennsylvania State University, the University of Missouri, the University of California, Irvine, and Purdue University.
[34] Collected in DOI:10.17909/SBX7-VG73.
[35] Our updated ephemeris reveals the transit midpoint to have been 2021 June 15 at UT 12:52 ± 0:03—unfortunately not visible from RBO, with the transit starting during morning twilight.

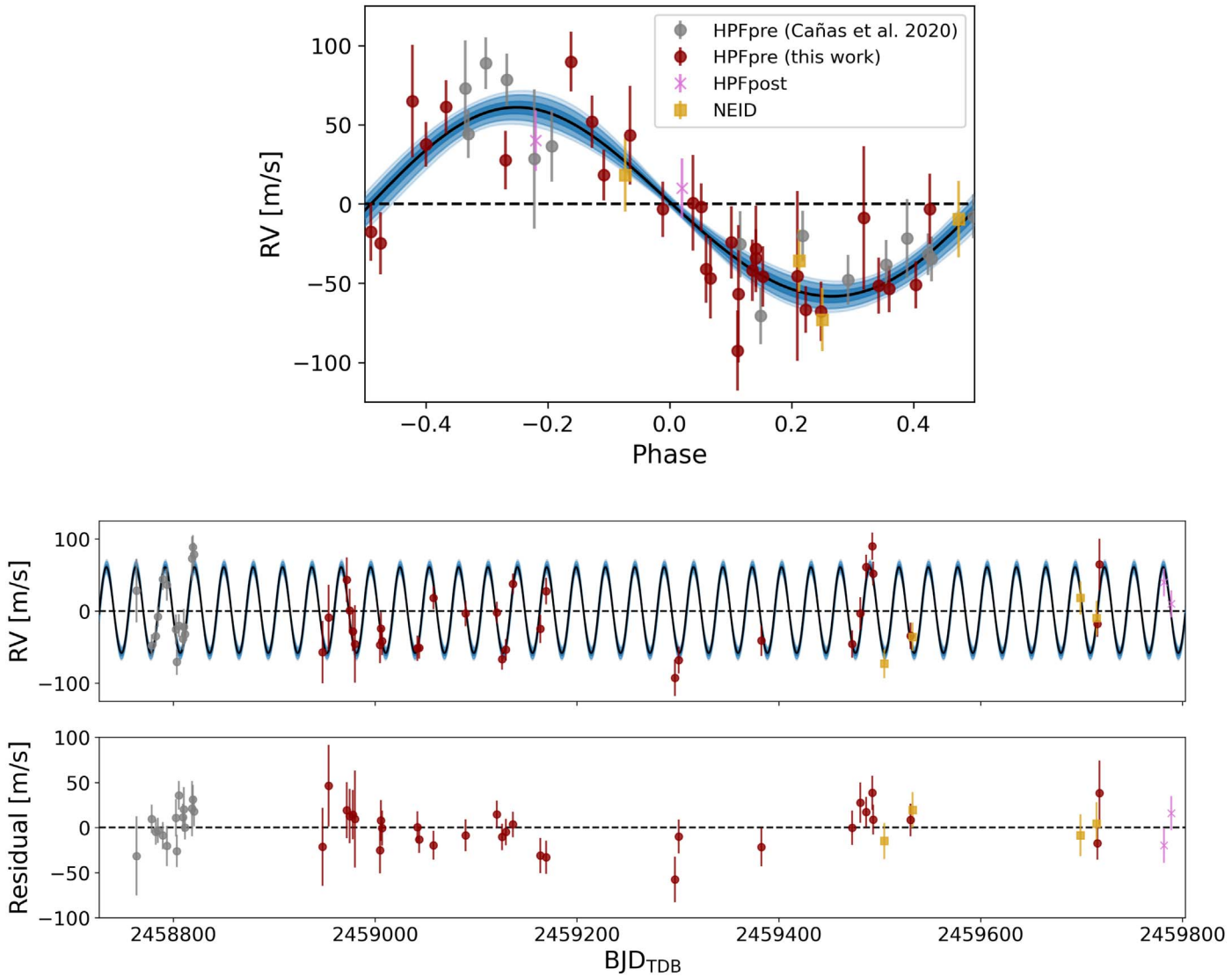

Figure 1. Joint-fit RVs of TOI-1899 b. The best-fit model is plotted as a black line, while the blue shaded regions denote the 1σ (darkest), 2σ, and 3σ ranges of the derived posterior solution. Top: phase-folded RVs, with HPF data from Cañas et al. (2020) in gray, new HPF data in dark red (pre-velocity break) and pink (post-velocity break), and NEID in gold. Bottom: unphased RVs and residuals as a function of time.

2.4.1. Perkin Observatory 17″ Telescope

We observed a partial transit of TOI-1899 b on the night of 2021 November 7 with the 17″ (0.43 m) PlaneWave Corrected Dall–Kirkham (CDK) telescope at the Richard S. Perkin Observatory at Hobart & William Smith Colleges. The processed data are shown in the top right panel of Figure 2; due to the long transit duration, we were only able to observe midtransit through egress.

The Perkin 17″ is mounted on a Paramount equatorial mount and equipped with an SBIG 8300 M camera at Cassegrain focus. The detector array is 3326 × 2504 pixels, with a field of view (FOV) of ∼21′ × 16′, resulting in an unbinned pixel scale of 0.″38 pixel^{-1}. We carried out our observations defocused to ∼4″ FWHM in Sloan Digital Sky Survey (SDSS) r', in 1 × 1 binning, with an exposure time of 180 s. The target started at an air mass of 1.02 and set to 1.85 over the course of our observations. We performed aperture photometry in `AstroImageJ` (`AIJ`; Collins et al. 2017), following the methodology outlined in Stefansson et al. (2017, 2018a). For our final `AIJ` reduction, we used an object aperture radius of 12 pixels (4.″6) and inner and outer sky radii of 30 and 45 pixels (11.″4 and 17.″1), respectively.

2.4.2. Davey Lab 24″ Telescope

On the same night (2021 November 7), we also observed TOI-1899 b with the 24″ (0.61 m) PlaneWave CDK located on the roof of Penn State's Davey Laboratory (Figure 2, bottom left panel). Similar to the Perkin observations above, we were only able to observe midtransit through egress.

The Davey Lab 24″ has an SBIG STX-9000 camera with an array of 3056 × 3056 pixels and an FOV of ∼32′ × 32′, corresponding to an unbinned pixel scale of 0.″63 pixel^{-1}. We carried out our observations defocused to ∼3″ FWHM in SDSS i', in 2 × 2 binning, with an exposure time of 30 s. During our observations, the target set from an air mass of 1.05 to 1.76. We reduced this photometry with `AIJ` in the same way as described above, with an object aperture radius of 6 binned pixels (7.″5) and inner and outer sky radii of 13 and 18 pixels (16.″2 and 22.″5), respectively.

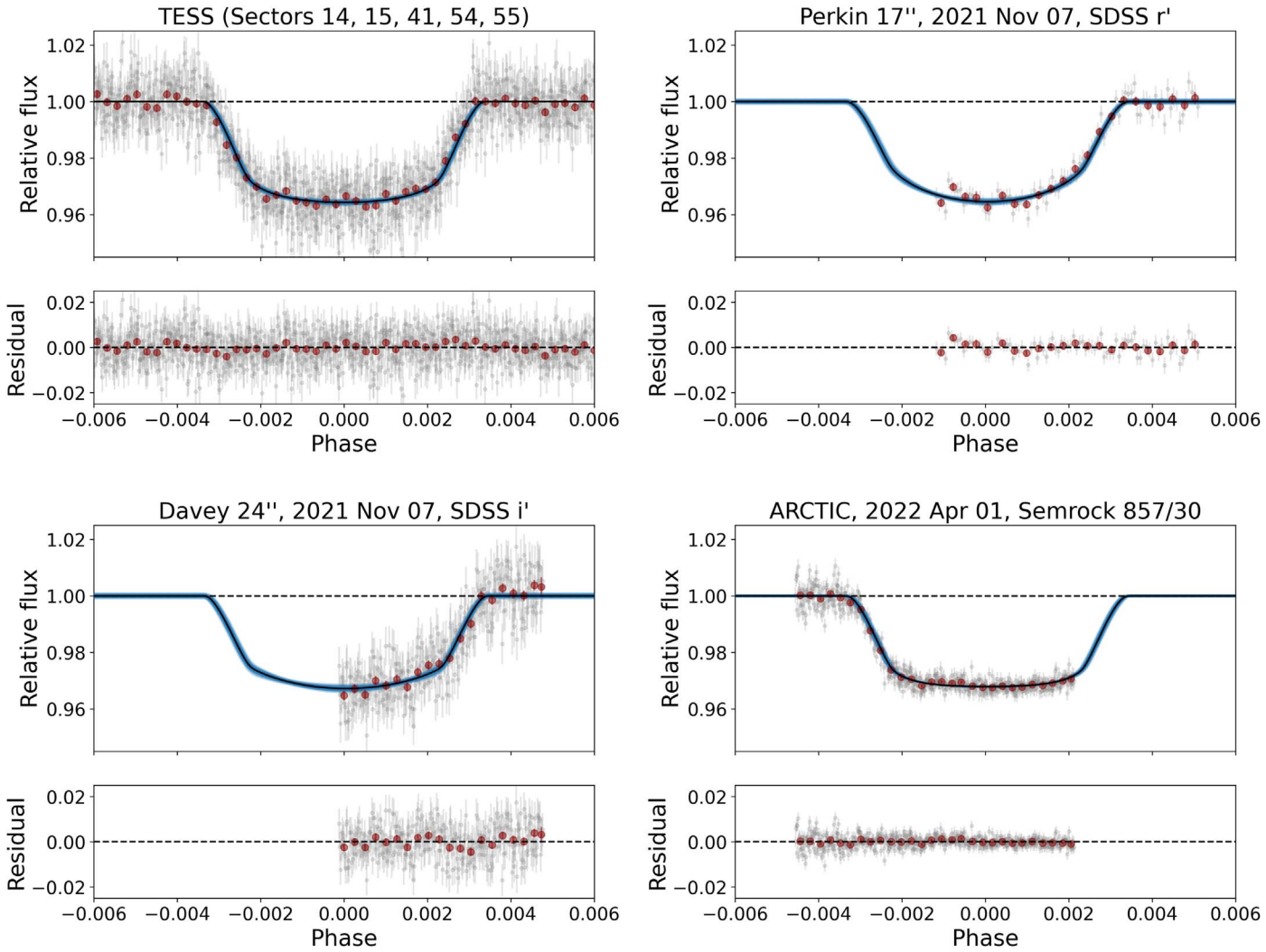

Figure 2. Joint-fit photometry of TOI-1899 b. In each panel, the best-fit model is plotted as a black line, while the blue shaded regions denote the 1σ (darkest), 2σ, and 3σ ranges of the derived posterior solution. We show transits from TESS (all available sectors, phase-folded; top left), the Perkin 17″ in SDSS r' (top right), the Davey 24″ in SDSS i' (bottom left), and ARCTIC in Semrock 857/30 (bottom right). Gray points are unbinned, while dark-red points have been binned to a cadence of 10 minutes. The photometry in this figure is available as Data Behind Figures.

(The data used to create this figure are available.)

2.4.3. ARCTIC

We also observed a partial transit of TOI-1899 b on the night of 2022 April 1[36] with the Astrophysical Research Consortium (ARC) Telescope Imaging Camera (ARCTIC; Huehnerhoff et al. 2016) on the ARC 3.5 m Telescope at Apache Point Observatory (Figure 2, bottom right panel). This time, we were able to observe ingress through midtransit but unable to catch egress owing to morning twilight.

We operated ARCTIC in the quad-amplifier and fast-readout modes, defocused to ∼5″ FWHM and binned 4×4 with an exposure time of 25 s. Since our observations began at very high air mass, we used a Semrock 857/30 filter—this narrow passband (842–872 nm) was chosen to avoid atmospheric absorption bands, minimizing the impact of clouds or high air mass on the photometry (Stefansson et al. 2017, 2018b). Over the course of the night, the target rose from its starting air mass of 6.11 to end at 1.10. For the `AIJ` reduction, we used an object aperture radius of 12 binned pixels (5.″4) and inner and outer sky radii of 20 and 25 pixels (9.″1 and 11.″4), respectively. We see a strong slope in the raw data from this night; without baseline available on both sides of the transit, we choose to detrend with a line and allow the dilution of this transit to float in our joint fit.

[36] We also attempted observations on this night from the Perkin 17″, the Davey Lab 24″, and the Peter van de Kamp Observatory at Swarthmore College, but we were unsuccessful owing to weather.

2.5. Archival Photometry

TOI-1899 b is a long-period planet in a crowded field, exemplifying a class of TESS planet candidates that can be difficult to validate. The short TESS sector lengths mean large uncertainties on the period—especially if only a single transit is detected, as was true when Cañas et al. (2020) initially validated TOI-1899 b—and the large size of TESS pixels on-sky leads to uncertainty about the true host star of the transit and the level of background contamination. Typically, these parameters are constrained through a combination of ground-based transits, which are difficult to schedule without a precise

period, and RVs, which are necessarily time intensive for long-period planets. However, it is possible to glean some of this valuable information from the archival data of long-running photometric surveys, especially for deep transits like those of gas giants around M dwarfs.

We thus investigate whether the transit of TOI-1899 b can be detected in photometry from the All-Sky Automated Survey for SuperNovae (ASAS-SN; Kochanek et al. 2017) and the Zwicky Transient Facility (ZTF; Masci et al. 2019). With a ∼29-day period, there is only a 0.7% chance that TOI-1899 b is in transit at any given time, but these surveys' years of coverage encompass hundreds of observations. We retrieve the publicly accessible data from ASAS-SN Sky Patrol in V and g (2015 February 24–2018 November 10 and 2018 April 12–2022 December 22, respectively) and ZTF DR17 in zr and zg (including data up through 2023 March 9) and phase them to the planetary ephemeris as derived in this paper. Figure 3 shows that, unfortunately, ASAS-SN does not have the photometric precision necessary to detect the transit, but we do see a dip in flux suggestive of a transit in ZTF, especially in the zr band.

In addition, TOI-1899 is among the subset of Gaia sources with epoch photometry available in DR3 (Gaia Collaboration et al. 2023). The idea of using epoch photometry from astrometric missions such as Gaia or Hipparcos to detect transiting exoplanets is not new—e.g., the recovery of HD 209458 b from Hipparcos data (Robichon & Arenou 2000), or the recent discoveries of Gaia-1 b and Gaia-2 b (Panahi et al. 2022)—but the excellent spatial resolution and photometric precision of Gaia also make it useful for validating TESS objects like TOI-1899 b. However, the cadence of Gaia data is much sparser, so one must be fortunate enough for an observation epoch to line up with the transit.

We retrieve the epoch photometry using the Gaia archive DataLink service,[37] discard any data that have been rejected by either the photometry or variability processing pipelines, and normalize the G, $G_{\rm RP}$, and $G_{\rm BP}$ bands separately to their median fluxes. The bottom panel of Figure 3 shows that the most significant drop in flux clearly lines up with the transit. If we only consider the $G_{\rm BP}$ photometry, we might dismiss this dip as random scatter, as we see similar excursions in flux at other orbital phases. However, the concurrent G photometry shows the same dip while exhibiting far less scatter overall, suggesting that this flux decrease is real and produced by the planetary transit.

While we do not include these data sets in our subsequent analysis owing to their large scatter and/or sparse cadence, we present this exercise to demonstrate that long-term photometric surveys and Gaia epoch photometry—when released for all sources in the upcoming DR4—can potentially be used to validate deep TESS transits, such as those of giant planet candidates around M dwarfs, and help refine ephemerides as a result of their longer time baselines.

3. Stellar Parameters

Initial stellar parameters for the host star TOI-1899 were derived by Cañas et al. (2020) using spectroscopic parameters from `HPF-SpecMatch` (Stefansson et al. 2020) as priors for an SED fit with the `EXOFASTv2` analysis package (Eastman et al. 2019). Since then, the `HPF-SpecMatch` spectral library has been expanded from 55 stars to 166, now spanning $T_{\rm eff} = 2700$–6000 K, $\log g = 4.29$–5.26, and $[{\rm Fe/H}] = -0.5$ to 0.5. Thus, we repeat the procedure outlined in Section 4.3 of Cañas et al. (2020) to rederive the stellar parameters.

`HPF-SpecMatch` is broadly based on the algorithms for `SpecMatch-Emp` outlined by Yee et al. (2017). In brief, it compares a high-S/N HPF spectrum of the target star to a library containing similarly high S/N spectra (also observed with HPF) of stars with well-characterized properties. Using χ^2 minimization, it produces a weighted linear combination of the five best-fitting library spectra, from which it determines the target's spectroscopic parameters. The errors are determined by a leave-one-out cross-validation, which estimates the properties of a library star of interest using all the other stars in the library; we take the difference between these derived values and the true values as the errors.

We use the single highest-S/N HPF spectrum of TOI-1899 to perform this comparison against the updated `HPF-SpecMatch` spectral library—taken on 2019 November 23, this happens to be the exact same spectrum used by Cañas et al. (2020) when they derived spectroscopic parameters from the old `HPF-SpecMatch` library. In the left panel of Figure 4, we show the spectra of the five best-fitting library stars across a portion of HPF order index 5 and the composite spectrum compared to that of TOI-1899.

We then repeat the subsequent SED fit (Figure 4, right panel) with `EXOFASTv2`, using the default MIST stellar models (Choi et al. 2016; Dotter 2016) and the priors listed in Table 2. We use the same priors as Cañas et al. (2020), apart from the new $T_{\rm eff}$, [Fe/H], and $\log g$ derived from the updated `HPF-SpecMatch` library and the addition of the Pan-STARRS DR2 gry photometry. We find that all derived stellar parameters are consistent with the values reported in Table 2 of Cañas et al. (2020). Nevertheless, we present the updated stellar parameters in Table 2 for completeness and adopt these new values for use in our joint fit.

3.1. Stellar Activity

With a total of 44 HPF RVs now spanning nearly 3 yr, we investigated whether these RVs were correlated with several common NIR activity indicators—the differential line width (dLW), the chromatic index (CRX; Zechmeister et al. 2018), and the Ca infrared triplet (Ca IRT; air wavelengths of 8498, 8542, and 8662 Å) indices. We found no strong correlations between the RVs and any of these activity metrics using the Kendall rank correlation coefficient (Kendall τ). We include the generalized Lomb–Scargle (GLS) periodograms and corner plot for the HPF RVs and activity indicators in Appendix A, with the activity index values available as Data Behind Figures. With only four NEID RVs, we do not have enough data to look for similar temporal correlations, but examination of the raw spectra shows no signs of emission in either the Hα line or the Na doublet.[38]

[37] Directly accessible at https://gea.esac.esa.int/data-server/data?retrieval_type=epoch_photometry&ID=Gaia+DR3+2073530190996615424&format=csv.

[38] While NEID's wavelength range also includes the Ca II H and K lines, we did not use them because these orders are very low S/N for a faint M dwarf like TOI-1899.

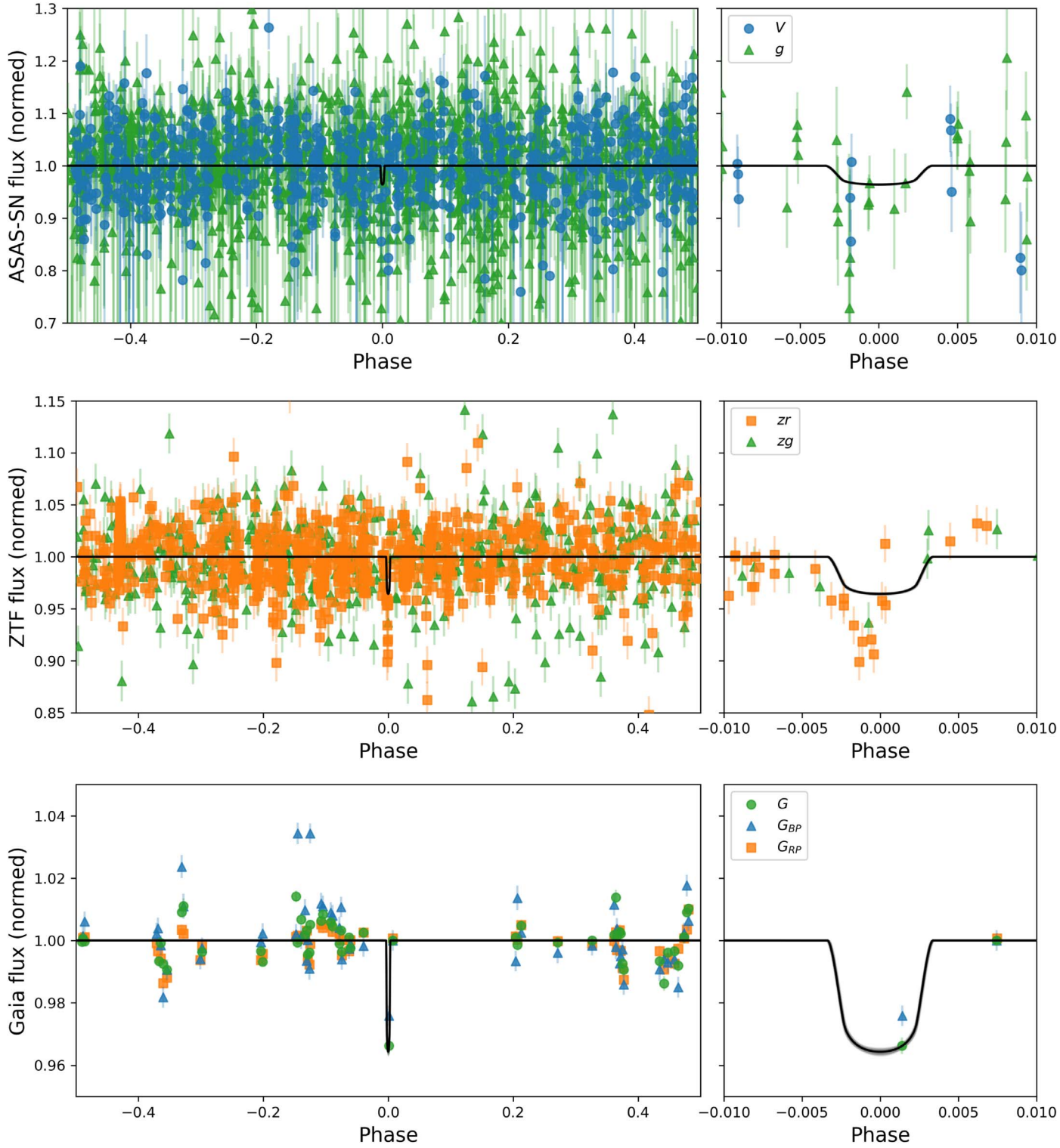

Figure 3. ASAS-SN, ZTF, and Gaia photometry phased to the ephemeris of TOI-1899 b, with the right panels zoomed in around the transit. The joint-fit model from Figure 2 is overplotted, including the 1σ, 2σ, and 3σ posteriors. ASAS-SN does not have the precision to detect the transit, but we see a potential transit in ZTF and a more definitive one in Gaia.

We note that in both HPF and NEID spectra all three lines of the Ca IRT appear to show consistent, low levels of emission in the line core, but this does not appear to have any significant effect on the RVs, as we see nearly no correlation between any of the Ca IRT indices and the HPF RVs ($\tau = 0.0023$–0.0035). Given that none of the other indicators we examined show signs of activity, we conclude that TOI-1899 is a quiet, low-activity M dwarf.

3.2. Stellar Rotation Period

In an effort to constrain the stellar rotation period, we examine the GLS periodograms of the previously mentioned HPF activity indicators (dLW, CRX, and Ca IRT). We find no signals with false-alarm probability (FAP) $< 0.1\%$. We do see peaks at the FAP $\sim 1\%$ level in the Ca IRT 3 (8662 Å) index,

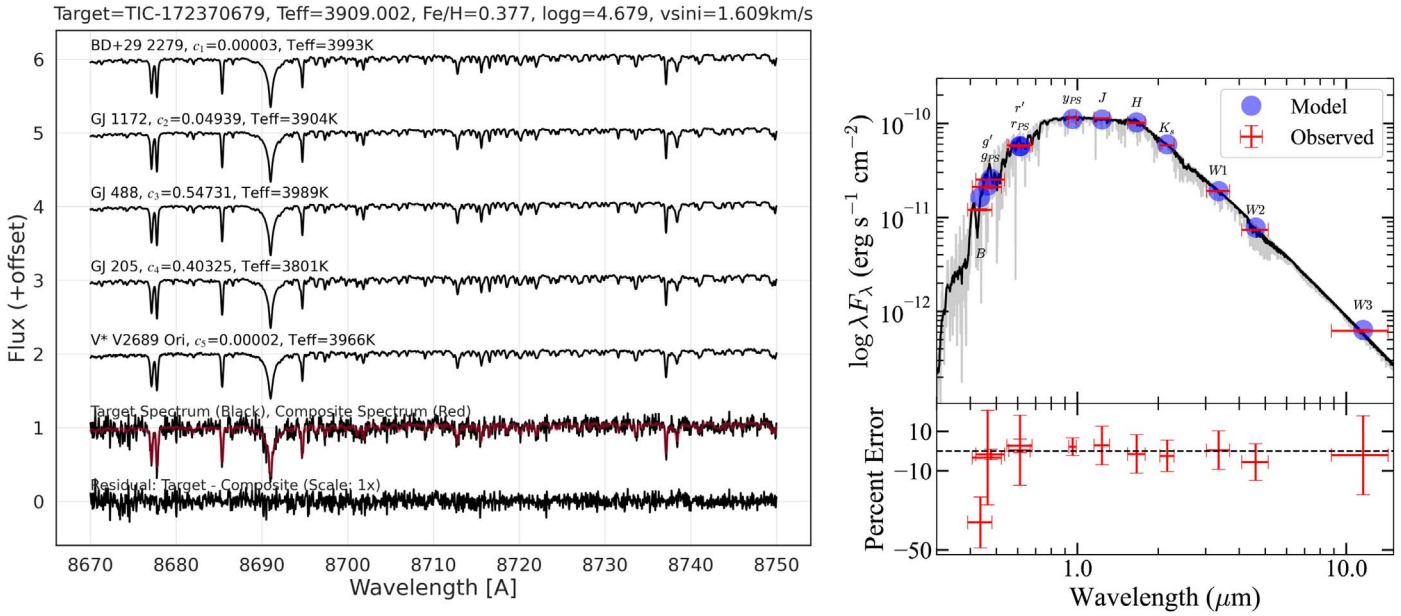

Figure 4. Left: spectra of the five best-matching `HPF-SpecMatch` library stars, with the composite library spectrum (red) overplotted against the highest-S/N observed spectrum of the target star TOI-1899. The composite spectrum is constructed using the weights c_i noted for each library star. Right: SED of TOI-1899 as fit by `EXOFASTv2`, showing the broadband photometric measurements (red; x-error bars indicate the passband width) and the derived MIST model fluxes (blue). A NextGen BT-SETTL model (Allard et al. 2012) is overlaid for reference (gray, smoothed version in black) and is not used as part of the SED fit.

Table 2
Summary of Updated Stellar Parameters

Parameter[a]	Units	Source	Cañas et al. (2020)	This Work	% Diff.[b]	σ Diff.[b]
Priors for `EXOFASTv2` SED Fit						
Spectroscopic parameters:						
Effective temperature	$T_{\rm eff}$ (K)	`HPF-SpecMatch`	3925 ± 77	3909 ± 88	–4.1	–0.21
Metallicity	[Fe/H] (dex)	`HPF-SpecMatch`	0.20 ± 0.13	0.38 ± 0.12	+90.0	+1.38
Surface gravity	$\log g$ (cgs)	`HPF-SpecMatch`	4.68 ± 0.05	4.68 ± 0.05	< 0.1	< 0.01
Photometric magnitudes:						
APASS Johnson B	B (mag)	Henden et al. (2015)	15.898 ± 0.029	same	⋯	⋯
APASS Sloan g'	g' (mag)	Henden et al. (2015)	15.115 ± 0.054	same	⋯	⋯
APASS Sloan r'	r' (mag)	Henden et al. (2015)	13.728 ± 0.040	same	⋯	⋯
Pan-STARRS $g_{\rm PS}$	$g_{\rm PS}$ (mag)	Chambers et al. (2016)	⋯	14.889 ± 0.006	⋯	⋯
Pan-STARRS $r_{\rm PS}$	$r_{\rm PS}$ (mag)	Chambers et al. (2016)	⋯	13.708 ± 0.008	⋯	⋯
Pan-STARRS $y_{\rm PS}$	$y_{\rm PS}$ (mag)	Chambers et al. (2016)	⋯	12.495 ± 0.010	⋯	⋯
2MASS J	J (mag)	Cutri et al. (2003)	11.342 ± 0.022	same	⋯	⋯
2MASS H	H (mag)	Cutri et al. (2003)	10.666 ± 0.022	same	⋯	⋯
2MASS K_s	K_s (mag)	Cutri et al. (2003)	10.509 ± 0.018	same	⋯	⋯
WISE W1	W1 (mag)	Wright et al. (2010)	10.412 ± 0.022	same	⋯	⋯
WISE W2	W2 (mag)	Wright et al. (2010)	10.460 ± 0.021	same	⋯	⋯
WISE W3	W3 (mag)	Wright et al. (2010)	10.312 ± 0.045	same	⋯	⋯
Other Priors						
Distance	d (pc)	Bailer-Jones et al. (2018)	128.4 ± 0.3	same	⋯	⋯
Maximum V extinction	A_V (mag)	Green et al. (2019)	0.02	same	⋯	⋯
Derived stellar parameters (used for joint RV + transit fit):						
Effective temperature	$T_{\rm eff}$ (K)	`EXOFASTv2`	3841^{+54}_{-45}	3926^{+45}_{-47}	+2.2	+1.57
Metallicity	[Fe/H] (dex)	`EXOFASTv2`	$0.31^{+0.11}_{-0.12}$	0.28 ± 0.11	–9.6	–0.25
Surface gravity	$\log g$ (cgs)	`EXOFASTv2`	$4.669^{+0.025}_{-0.022}$	$4.672^{+0.021}_{-0.020}$	+0.1	+0.12
Mass	M_* ($M_\odot$)	`EXOFASTv2`	$0.627^{+0.026}_{-0.028}$	$0.632^{+0.026}_{-0.025}$	+0.7	+0.19
Radius	R_* ($M_\odot$)	`EXOFASTv2`	$0.607^{+0.019}_{-0.023}$	$0.607^{+0.017}_{-0.016}$	< 0.1	< 0.01
Density	ρ_* (cgs)	`EXOFASTv2`	$3.95^{+0.37}_{-0.29}$	$3.98^{+0.29}_{-0.27}$	+0.7	+0.08
Age	Age (Gyr)	`EXOFASTv2`	$7.4^{+4.4}_{-4.6}$	$7.1^{+4.5}_{-4.8}$	–4.1	–0.07
V-band extinction	A_V (mag)	`EXOFASTv2`	0.010 ± 0.007	0.010 ± 0.007	< 0.1	< 0.01

Notes.
[a] See Table 3 in Eastman (2017) for a detailed description of all parameters.
[b] Values from Cañas et al. (2020) used as the fiducial.

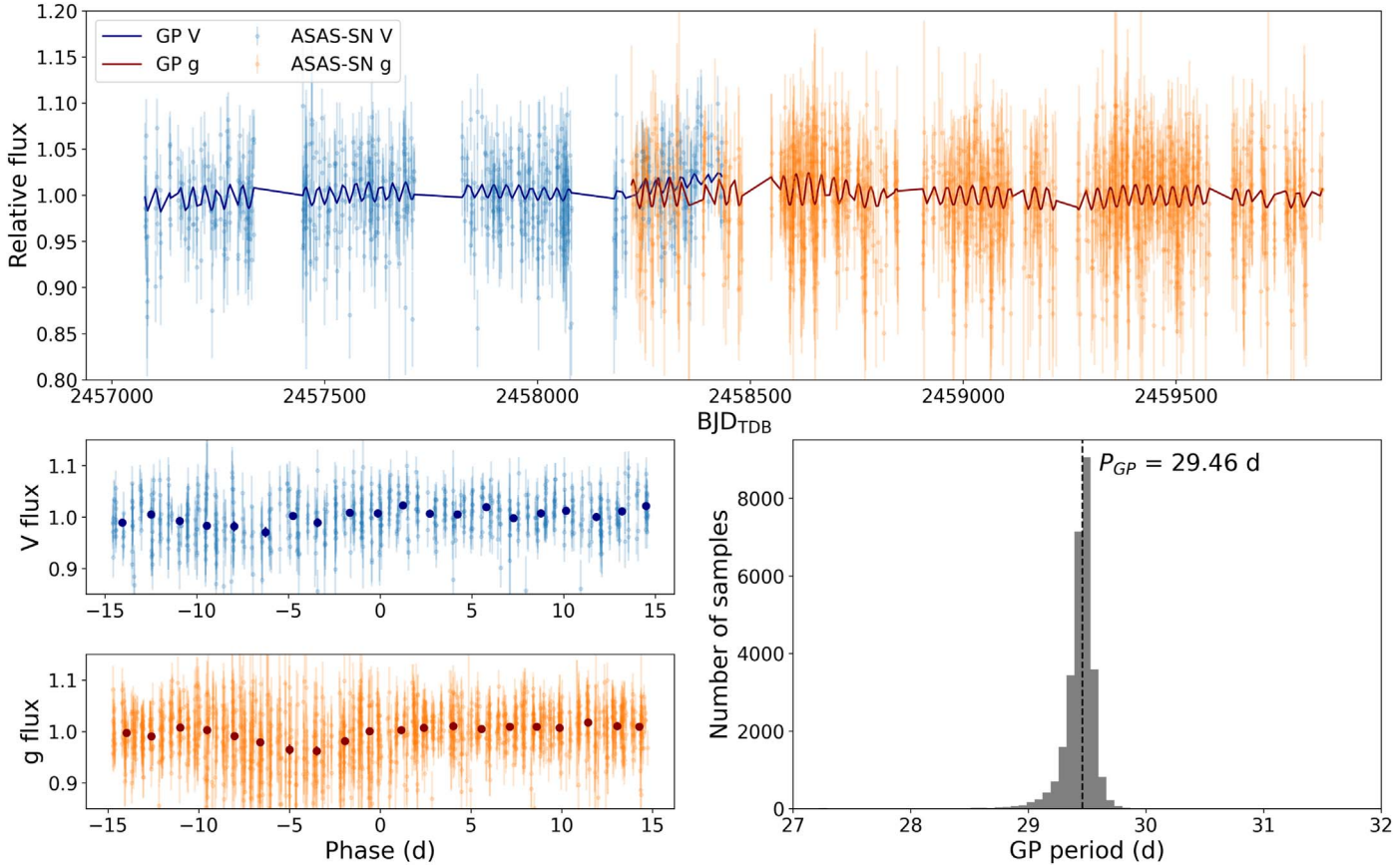

Figure 5. Top: ASAS-SN photometry fit with a `celerite` quasi-periodic kernel, suggesting a stellar rotation period of $29.46^{+0.07}_{-0.10}$ days. Bottom left: photometry phased to the derived GP period. Dark points have been binned to better show the flux variation as a function of phase. Bottom right: histogram of posterior samples for P_{GP}.

with periodicities ∼80 and ∼100 days, but it is doubtful whether these peaks correspond to rotationally modulated activity, as they are not corroborated by any other activity indicator—including the other two Ca IRT indices.

We also search for rotationally modulated photometric variability in the TESS photometry, as well as the publicly accessible photometry from ASAS-SN and ZTF (as mentioned in Section 2.5). Since the ASAS-SN V and g photometries share only a small time baseline overlap and the bandpasses are similar, we also try combining these data sets to see whether this boosts the significance of long-period signals. We include the GLS periodograms for ASAS-SN (V, g, and combined), ZTF (zr and zg), and TESS in Appendix B.

From the combined ASAS-SN $V+g$ periodogram (Figure 12), we detect multiple peaks around $P \sim 27$–29 days with FAP <0.1%. A similar period ($P \sim 31$ days) is suggested by ZTF zr (Figure 13), albeit with considerable aliasing as a result of the window function. Unfortunately, these peaks cannot be corroborated by the TESS PDCSAP photometry, which is unreliable when used to detect photometric variability on periods $\gtrsim$10 days, as a result of co-trending performed by the PDC processing (as discussed by, e.g., Claytor et al. 2022).

However, the TESS light curves can still be used to search for signs of shorter-period variability. We find many broad peaks in the regime with a period of $P \sim 4$–15 days that are all formally highly significant (FAP $\ll$0.1%), but we also observe that these periods change from sector to sector, including back-to-back sectors (most strikingly, Sectors 54 and 55 in Figure 14). Therefore, we find it unlikely that the observed photometric variability in TESS PDCSAP is directly tracing the stellar rotation period, which should remain constant. In addition, neither ASAS-SN nor ZTF finds any strong evidence of periodicity in the 4-to-15-day period range, even though these data sets should have the requisite sampling to detect them. Furthermore, we do not see these peaks when applying the systematics-insensitive periodogram from `TESS-SIP` (Hedges et al. 2020), which attempts to detrend out the effects of TESS instrumental systematics such as scattered light. Using either the target pixel files (TPFs) or light-curve files (LCFs), we find that the strongest peaks in the `TESS-SIP` periodogram line up with excess power in background pixels (Figure 15), suggesting that their cause is an instrumental effect not limited to our target star.

Since the ASAS-SN data are the best behaved and longest running (spanning ∼7 yr) of our photometric data sets, we also attempt to fit a Gaussian process (GP) to it using the `celerite` quasi-periodic kernel (Foreman-Mackey et al. 2017) with the period shared between the V and g photometries, using a uniform prior from 1 to 100 days (Figure 5). The quasi-periodic GP fit yields a period of $29.46^{+0.07}_{-0.10}$ days for the photometric modulation—intriguingly close to the orbital period of TOI-1899 b.

This is also very close to the lunar synodic period of 29.53 days. We do not see power in the window function at this period, suggesting that the detected period is not a consequence of the observing cadence, though it is possible that lunar contamination could produce periodic photometric variations. We tentatively adopt this as the stellar rotation period, noting

Table 3
Derived Parameters for the TOI-1899 System

Parameter	Units	Cañas et al. (2020)	This Work	% Diff.[b]	σ Diff.[b]
Orbital parameters:					
Orbital period	P (days)	$29.02^{+0.36}_{-0.23}$	$29.090312^{+0.000036}_{-0.000035}$	+0.2	+0.20
Eccentricity	e	$0.118^{+0.073}_{-0.077}$	$0.044^{+0.029}_{-0.027}$	–62.7	–0.96
Argument of periastron	ω (degrees)	-13^{+27}_{-28}	-53^{+42}_{-36}	⋯	–1.42
Semiamplitude velocity	K (m s^{-1})	$59.91^{+6.41}_{-6.32}$	$59.82^{+3.52}_{-3.49}$	–0.2	–0.01
$\mathrm{HPF_{pre}}$ RV offset	γ_{HPFpre} (m s^{-1})	$16.64^{+5.39}_{-5.23}$	$24.32^{+2.49}_{-2.55}$	+46.2	+1.42
$\mathrm{HPF_{pre}}$ RV jitter	σ_{HPFpre} (m s^{-1})	$0.39^{+3.84}_{-0.36}$	$7.90^{+4.83}_{-4.94}$	+1925.6	+1.96
$\mathrm{HPF_{post}}$ RV offset	$\gamma_{\mathrm{HPFpost}}$ (m s^{-1})	⋯	$-50.35^{+18.22}_{-14.74}$	⋯	⋯
$\mathrm{HPF_{post}}$ RV jitter	$\sigma_{\mathrm{HPFpost}}$ (m s^{-1})	⋯	$2.47^{+25.34}_{-2.39}$	⋯	⋯
NEID RV offset	γ_{NEID} (m s^{-1})	⋯	$-1.49^{+10.80}_{-10.63}$	⋯	⋯
NEID RV jitter	σ_{NEID} (m s^{-1})	⋯	$18.39^{+13.51}_{-6.97}$	⋯	⋯
Transit parameters:					
Time of conjunction	T_C ($\mathrm{BJD_{TDB}}$)	$2458711.957792^{+0.001182}_{-0.001179}$	$2458711.959171^{+0.001116}_{-0.001105}$	⋯	+1.16
Scaled radius	R_p/R_*	$0.194^{+0.004}_{-0.005}$	0.168 ± 0.003	–13.4	–5.20
Scaled semimajor axis	a/R_*	$56.22^{+1.59}_{-1.66}$	$54.01^{+1.78}_{-1.52}$	–3.9	–1.33
Orbital inclination	i (deg)	$89.77^{+0.15}_{-0.14}$	$89.64^{+0.07}_{-0.08}$	–1.4	–0.92
Impact parameter	b	$0.22^{+0.15}_{-0.14}$	0.35 ± 0.07	+59.1	+0.86
Transit duration	T_{14} (hours)	$4.67^{+0.12}_{-0.10}$	4.70 ± 0.04	+0.6	+0.25
Photometric jitter, TESS	σ_{TESS} (ppm)	$0.01^{+5.62}_{-0.01}$	$0.02^{+4.16}_{-0.02}$	+100.0	< 0.01
Dilution, TESS	D_{TESS}	1	1.086 ± 0.025	+8.6	⋯
Photometric jitter, Perkin	σ_{Perkin} (ppm)	⋯	2360^{+300}_{-260}	⋯	⋯
Photometric jitter, Davey	σ_{Davey} (ppm)	⋯	5090^{+330}_{-340}	⋯	⋯
Photometric jitter, ARCTIC	σ_{ARCTIC} (ppm)	⋯	2010^{+80}_{-70}	⋯	⋯
Dilution, ARCTIC	D_{ARCTIC}	⋯	1.002 ± 0.021	⋯	⋯
Planetary parameters:					
Mass	M_p (M_J)	0.66 ± 0.07	0.67 ± 0.04	+1.5	+0.14
Radius	R_p (R_J)	$1.15^{+0.04}_{-0.05}$	0.99 ± 0.03	–13.9	–3.20
Density	ρ_p (g cm^{-3})	$0.54^{+0.09}_{-0.10}$	0.85 ± 0.10	+57.4	+3.44
Surface gravity	$\log g_p$ (cgs)	$3.095^{+0.053}_{-0.056}$	$3.191^{+0.039}_{-0.041}$	+3.1	+1.81
Semimajor axis	a (au)	$0.1587^{+0.0067}_{-0.0075}$	$0.1525^{+0.0065}_{-0.0060}$	–3.9	–0.82
Average incident flux	$\langle F \rangle$ (10^8 erg s^{-1} cm^2)	0.039 ± 0.003	$0.046^{+0.004}_{+0.003}$	+17.9	+2.33
Equilibrium temperature[a]	T_{eq} (K)	362 ± 7	378^{+8}_{-7}	+4.4	+2.28

Notes.
[a] The planet is assumed to be a blackbody.
[b] Values from Cañas et al. (2020) used as the fiducial.

that it would be consistent with the lack of visible broadening in either the HPF or NEID spectra, which indicates $v \sin i \lesssim 2$ km s^{-1}.

4. Joint Fitting of Transit and RV Data

We jointly model the photometry and RVs using `juliet` (Espinoza et al. 2019), which relies on `batman` (Kreidberg 2015) for the photometric modeling and `radvel` (Fulton et al. 2018) for the RV modeling. The photometric transit model is based on that of Mandel & Agol (2002) and uses the q_1 and q_2 parameterization from Kipping (2013) for the quadratic limb-darkening law. `juliet` uses the dynamic nested sampling package `dynesty` (Speagle 2020) to perform its parameter estimation. We model the RVs using a standard Keplerian model and allow the eccentricity to float. For the joint fitting of the photometry and RVs, we also include a simple white-noise model in the form of a jitter term that is added in quadrature to the measurement errors from each data set.

For the transit model, we fix the dilution of the Perkin and Davey transits to 1 and allow dilution to float for TESS and ARCTIC. We observed heavy systematics in the raw ARCTIC data, which we attempted to detrend out—but without having baseline on both sides, we were not confident that this data set accurately reflected the true transit depth. We also experimented with allowing the TESS dilution and noise properties to float independently for each sector, since TOI-1899 lies in a crowded field where the background stellar contamination will realistically change from sector to sector. However, we found that this introduced too many free parameters, making it very difficult for the joint fit to converge, so in our final `juliet` fit we group together all five sectors of TESS data as a single instrument with shared limb-darkening, dilution, and noise parameters. In addition, we include a GP using the quasi-periodic kernel from `celerite` (Foreman-Mackey et al. 2017) for the TESS data in order to fit for correlated noise.

We present the joint fit to our RVs and transit photometry in Figures 1 and 2, respectively, and the final derived planet parameters in Table 3, with the values from Cañas et al. (2020) shown for comparison. Our results broadly agree with the earlier-derived parameters, with the additional transit observations greatly increasing the precision on the orbital period. We note that the RV jitter term, σ_{HPFpre}, is somewhat higher in our

fit, possibly since the orbital period is now tightly constrained by the transits, whereas it was free to float in the single-transit solution.

Notably, our fit yields a smaller planetary radius of $(0.99 \pm 0.03)R_J$, compared to the earlier radius estimate of $1.15^{+0.04}_{-0.05}\ R_J$, with corresponding increases in density and surface gravity. We believe that the previous radius value was inflated owing to overcorrection of dilution in TESS Sectors 14 and 15, as there were no ground-based transit data available at the time. We find an overall TESS dilution factor of $D_{TESS} = 1.086$. This effect has been seen before in, e.g., Burt et al. (2020), who found a 13% difference in derived planetary radius as a result of properly accounting for the TESS dilution overcorrection. This is supported by our reanalysis of the TESS photometry using the TESS-Gaia Light Curve package (`tglc`; Han & Brandt 2023), which uses Gaia DR3 source positions and brightnesses to construct a model of the TESS point-spread function (PSF), and it uses this to perform PSF photometry on the full-frame images (for details see Sections 3 and 4.1 of Han & Brandt 2023). A photometric fit to the `tglc`-processed TESS light curve yields a scaled planetary radius of $R_p/R_* = 0.169 \pm 0.004$ (corresponding to $R_p = (0.99 \pm 0.03)R_J$), which is fully consistent with the radius derived from ground-based photometry. The new radius brings TOI-1899 b in line with the size expected from Jovian-planet models, resolving previous concerns about unaccounted-for inflation mechanisms in this planet (Müller & Helled 2023).

We use `thejoker` (Price-Whelan et al. 2017) to put constraints on the presence of long-period, coplanar companions from the HPF RV residuals. We put a 3σ upper limit of $0.54M_J$ ($K = 36\ m\ s^{-1}$) on companion objects within 1 au and $1.16M_J$ ($K = 49\ m\ s^{-1}$) within 2 au. TOI-1899 b thus appears to be isolated from other massive planets in its system, if they exist at all. Though we can neither confirm nor rule out the presence of small companion planets like those commonly found alongside FGK WJs, the low eccentricity of TOI-1899 b seems to suggest a similar dynamically cool formation method.

5. Discussion

We show in Figure 6 that TOI-1899 b presents a unique opportunity to study a planet that spans multiple regions of currently unexplored parameter space. It belongs to the small but steadily growing population of gas giants orbiting M dwarfs, though TOI-1899 b has by far the longest period of these planets and is therefore the only one with an equilibrium temperature < 400 K. How this planet formed and why it seems to be the only known transiting Jovian planet around an M dwarf with $P > 10$ days is unclear—characterizing its atmosphere could provide insights surrounding TOI-1899 b's formation and evolutionary history.

5.1. Prospects for Atmospheric Characterization

We calculate a Transmission Spectroscopy Metric (TSM; Kempton et al. 2018) of 47, putting TOI-1899 b into the third quartile for promising follow-up candidates according to Kempton et al. (2018). However, as TSM is proportional to equilibrium temperature, it is no surprise that the cooler ($T_{eq} \approx 380$ K, albedo ≈ 0) TOI-1899 b possesses a lower TSM than hotter planets of similar size. In comparison with other Jovian planets of similar T_{eq}, however, TOI-1899 b has among the highest TSMs and a uniquely cool host star.

We simulate a cloud-free $10\times$ solar metallicity atmosphere model for TOI-1899 b using `ExoTransmit` (Kempton et al. 2017) assuming an isothermal P–T profile of 400 K, equilibrium chemistry (Figure 7, left), and uniform heat redistribution, as TOI-1899b is unlikely to be tidally locked. Combining this model with `PandExo` (Batalha et al. 2017), we simulate a JWST/NIRSpec-Prism transmission spectrum based on observations of two transits. As shown in Figure 7, under these atmospheric conditions we could detect methane and water features with $>4\sigma$ confidence. Using the same model assumptions, we also simulate a 300 K planet with an albedo of 0.5, finding that the differences in the observed spectra are negligible and yield the same expected molecular features.

Aerosols (condensation clouds and photochemically created hazes) appear to be a common feature in most exoplanet spectra (Madhusudhan 2018). Dymont et al. (2022) compared the presence of aerosols (derived from the water absorption feature strength in the Hubble/Wide Field Camera 3 bandpass) to a variety of stellar and planetary parameters for a set of 23 Neptunes and sub-Neptunes. Notably, the three planets observed by HST with temperatures between 300 and 500 K all show featureless spectra. While none of the planets analyzed by Dymont et al. (2022) are Jovian, we nonetheless expect aerosols to be present in TOI-1899 b's atmosphere. We also include two cloudy models in Figure 7—one with an opaque cloud deck (gray absorbers, wavelength independent) at pressure levels of 1.0 and 0.1 mbar. For the 1.0 mbar cloudy model, we calculate a 9σ significance of this model compared to a featureless flat line, with individual methane and water features detected to 3σ. These pressure levels were arbitrarily chosen to illustrate the precision JWST could achieve. Future work using photochemically motivated haze models (e.g., `VULCAN`; Tsai et al. 2017) would provide new insights into haze formation of a cool Jovian world.

While most relevant for rocky exoplanets with small-amplitude atmospheric features, the complicating effects of stellar contamination on abundance retrievals should not be ignored (e.g., Barclay et al. 2021, who show that this effect could produce the water signature seen in the atmosphere of K2-18 b), especially for M-dwarf hosts with molecular features in their atmospheres (Libby-Roberts et al. 2022). The presence of stellar surface inhomogeneities (e.g., starspots) can cause discrepancies in the transit depth as a function of wavelength (Rackham et al. 2018). Fortunately, TESS photometry of TOI-1899 shows no large-amplitude photometric modulations, and we show in Section 3.1 that activity indices in both HPF and NEID spectra show no strong correlations with RVs, indicating that TOI-1899 is a relatively quiet and low-activity star. Therefore, any stellar contamination is likely to be minimal compared with the expected larger planetary signal.

Retrieving water and methane abundances with a JWST spectrum would provide a C/O ratio for TOI-1899 b—a potential measurement for constraining the disk location where TOI-1899 b formed based on snowlines (Öberg et al. 2011; Brewer et al. 2017). Currently TOI-1899 b lies inside its star's snowline. Understanding whether this planet formed in situ or migrated inward would provide a key insight into the formation of the uncommon M-dwarf gas giants. We have constrained TOI-1899 b's mass and radius to $>10\sigma$ precision; thus, uncertainties in abundance retrievals will be dominated by JWST instrumental effects and the presence of aerosols, not from unconstrained planetary parameters (Batalha et al. 2019).

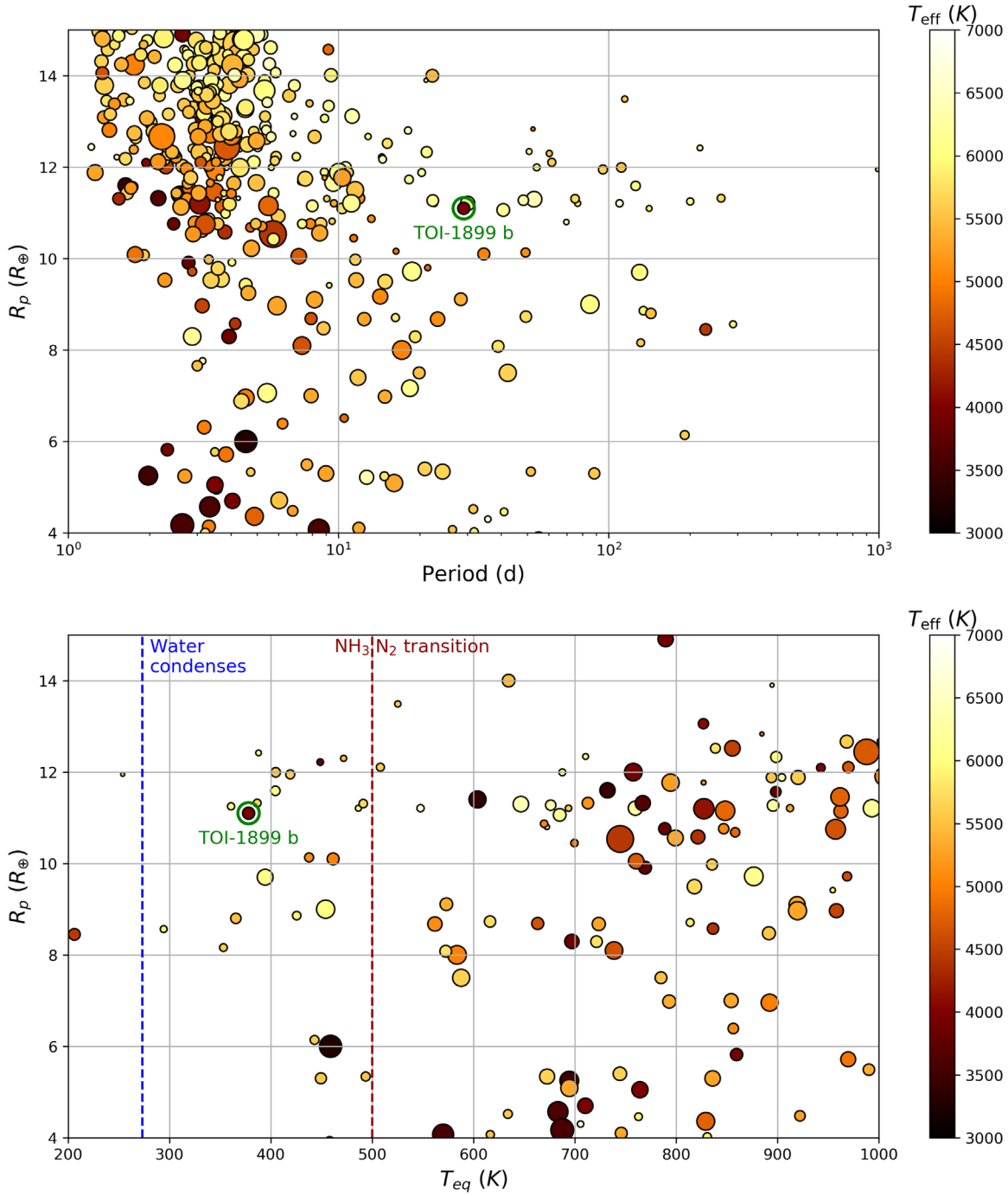

Figure 6. All transiting planets with masses measured to $>5\sigma$, plotted by planetary radius (R_p) vs. orbital period (P) (top) and planetary radius (R_p) vs. equilibrium temperature ($T_{\rm eq}$) (bottom). TOI-1899 b is circled in green. Points are colored by the host star $T_{\rm eff}$ and scaled in size by the planet's TSM (Kempton et al. 2018). We also highlight the transition temperatures for water vapor and ammonia, species whose presence or absence in the atmospheres of cool planets like TOI-1899 b may hint at their formation and cooling history (Fortney et al. 2020). TOI-1899 b is unique in R_p–P space in being the only M-dwarf Jupiter with $P > 10$ days, and in R_p–$T_{\rm eq}$ space by having among the highest TSMs of Jovian-sized planets with $T_{\rm eq} = 300$–500 K, while also being the only one whose host star has $T_{\rm eff} \lesssim 4000$ K. Data were retrieved from the NASA Exoplanet Archive (NASA Exoplanet Science Institute 2020) on 2023 May 15.

5.2. Tidally Induced Evolution

Temperate Jupiters such as TOI-1899 b would not be expected to experience significant tidal effects. However, since the host star is an M dwarf and the planet's orbital period is ∼29 days, the tidal evolution for this system can occur over timescales that are an order of magnitude larger than for short-period planets (Dobbs-Dixon et al. 2004; Barker & Ogilvie 2009; Rodríguez & Ferraz-Mello 2010; Alvarado-Montes & García-Carmona 2019) and four orders of magnitude larger than for ultra-short-period planets (Brown et al. 2011; Wong et al. 2016; McCormac et al. 2019; Alvarado-Montes et al. 2021).

In this section we show that TOI-1899 b does not exchange a significant amount of angular momentum with its host star, and thus the stellar rotation will not spin up because of the presence of the planetary companion. In consequence, the tidal evolution of TOI-1899 b will take too long to be significant within

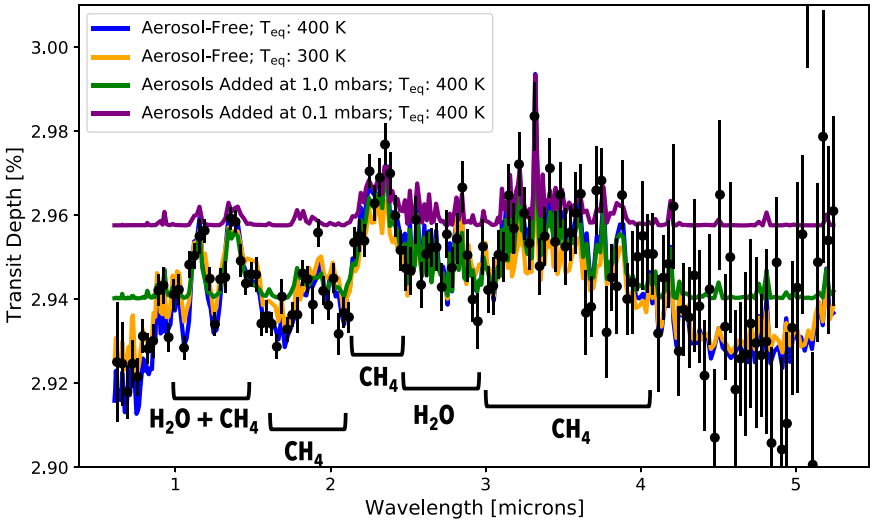

Figure 7. Simulated JWST/NIRSpec-Prism transmission spectrum ($R \sim 100$) of TOI-1899 b created using a 10× solar metallicity cloud-free atmosphere assuming a equilibrium temperature of 400 K and albedo of 0 (blue) generated with `ExoTransmit` (Kempton et al. 2017). Error bars are calculated using `PandExo` (Batalha et al. 2017) assuming two observed transits of TOI-1899 b. The planetary spectrum is dominated by the absorption features of methane and water in this bandpass. We plot the same model atmosphere with the addition of an opaque cloud deck (gray absorber) at pressure levels of 1.0 mbar (green) and 0.1 mbar (purple) for comparison. As TOI-1899 b may have a similar atmosphere to Jupiter, we also consider a higher albedo of 0.5, leading to an equilibrium temperature of 320 K (300 K for `ExoTransmit` grid; orange). The difference in temperature does not significantly change the spectra and should not impact JWST's ability to retrieve atmospheric abundances.

$\sim$13.5 Gyr, unless the host star has a small initial rotation period, $P_{\rm rot\_ini,\star}$ (Figure 8, top panel).

Nevertheless, since tidal evolution depends on the gravitational forces between the interacting bodies, the study of this type of close-in giant planet orbiting an M dwarf is necessary to analyze any deviation from the expected behavior of current theories of gravity, as has been done for other systems (Matsumura et al. 2010). In addition, in some cases tidal interactions can produce eccentric orbits, so studying these systems can help us construct the path for any future study of their atmospheric dynamics (Leconte et al. 2015).

Adopting the tidal formalism presented in Alvarado-Montes et al. (2021), we study the orbital migration of TOI-1899 b until the stellar forces overcome the planet's self-gravity at the Roche limit (Roche 1849)—where the planet starts being physically disrupted (Guillochon et al. 2011). As the planet decays in its orbit, we also integrate the stellar and planetary tidal dissipation reservoirs[39] (TDRs; Ogilvie 2013; Guenel et al. 2014), which provide insight into the exchange of angular momentum in the system. The top panel of Figure 8 shows the evolution of the planet semimajor axis for different initial stellar rotation periods, $P_{\rm rot\_ini,\star}$. For $P_{\rm rot\_ini,\star} \lesssim 7$ days, TOI-1899 b undergoes orbital decay and crosses the Roche limit in less than 13.5 Gyr.

Assuming the observed orbital eccentricity as the initial value, we studied the forward tidal evolution of TOI-1899 b for a wide range of stellar rotation periods spanning up to 29.5 days (see Section 3.2). We found that orbital circularization timescales are only sensible for $P_{\rm rot\_ini,\star} \lesssim 7$ days (Figure 8, middle panel), whereas longer $P_{\rm rot\_ini,\star}$ led to the damping of the planet's eccentricity in timescales that are too long and prevent the planet from undergoing orbital decay.

For the planet, we assume Jupiter-like values for the core's rigidity (4.46×10^{10} Pa; Lainey et al. 2009) and for the interior mass and radius aspect ratios (i.e., $\alpha_p = 0.126$ and $\beta_p = 0.02$; Mathis 2015). This yields a $k_{2,p}/Q_p \approx 10^{-4}$ when the planet is tidally locked, which is unlikely for a 29-day orbital period. That, however, does not affect the overall evolution of the system because $k_{2,\star}/Q_\star$ are the overarching parameters that drive tidal dissipation. For the star, we adopt $\alpha_\star$ and $\beta_\star$ from Gallet et al. (2017), where the interior aspect ratios are presented for different types of stars. The adopted values give us $k_{2,\star}/Q_\star$ ranging from 10^{-7} to 10^{-9}, for $P_{\rm rot\_ini,\star}$ equal to 3 and 29.5 days, respectively.

In general, the star becomes less dissipative with time (i.e., small values of $k_{2,\star}/Q_\star$) owing to the slow exchange of rotational (star) and orbital (planet) angular momentum, causing the stellar rotation period to increase (red line in Figure 9). As shown by the black line in Figure 9, during the first $\sim$20 Gyr of evolution the stellar wind braking rate increases, due mainly to the initial shrinking of the planetary orbit. However, the loss of material via stellar wind is the dominant mechanism for the evolution of the stellar rotation.

Given the initial distance of TOI-1899 b from the host star, we assume here that all tidal energy goes into circularizing the orbit and inducing orbital decay. Thus, during the tidal evolution of the system, we followed Fortney et al. (2007) to study the size contraction of TOI-1899 b. As shown by the bottom panel of Figure 8, for migration times less than 20 Gyr the planet contracts to $\sim$35% its initial radius, whereas for migration times larger than 20 Gyr the planet's size decreases to $\sim$42% its original size. Although this affects $k_{2,p}/Q_p$, which contributes to the overall exchange of angular momentum (since it depends on the planet's physical structure), the overarching tidally induced migration is commanded by the energy dissipated from the star's interior, which keeps constantly decreasing while the planet reaches a new orbital position. Such asymptotic decay with no crossing of the Roche limit occurs for $P_{\rm rot\_ini,\star} \gtrsim 7$ days.

It is worth mentioning that the tidal analysis performed here for TOI-1899 b has slightly different migration timescales depending on the amount of angular momentum driven by the

[39] Represented by k/Q, the imaginary part of the second-order Love number that quantifies the system's tidal dissipation.

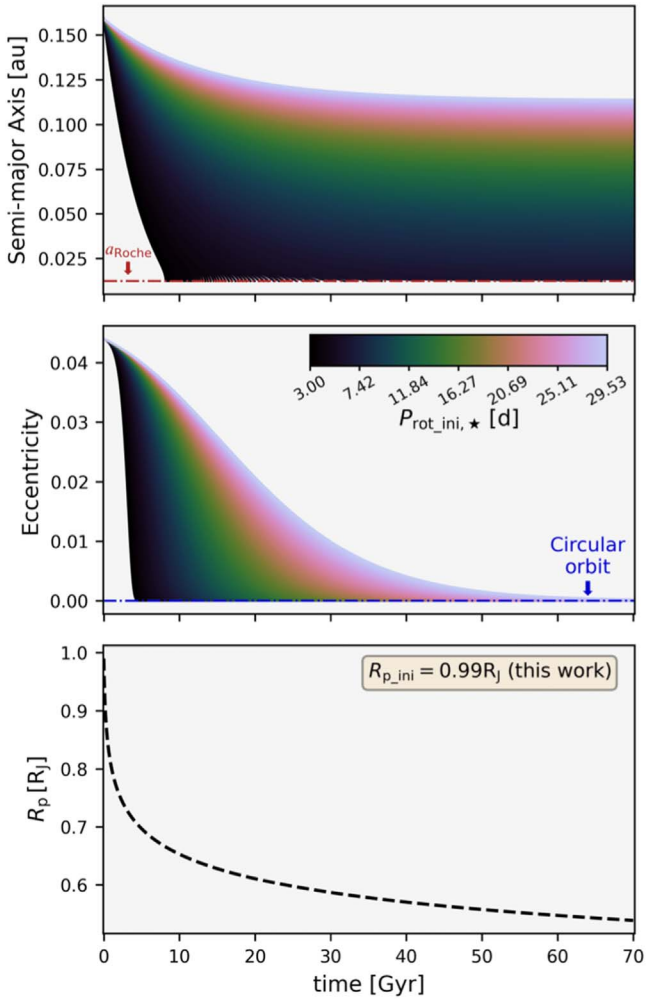

Figure 8. Top: orbital semimajor axis, a, as a function of time. The colors represent different initial stellar rotation periods, and the red dashed–dotted line stands for the system's Roche limit. Middle: change in the eccentricity, e, for each a on the top panel. Bottom: evolution of planetary radius, R_p, over the timescales of tidally induced migration.

envelope of the host star. This is represented by the product of $\zeta_\star$, the stellar gyration radius, and $\varepsilon_\star$, the fraction of the stellar envelope partaking in the exchange of angular momentum.[40] The product $\zeta_\star\varepsilon_\star$ will modify the times at which orbital decay occurs: in our analysis we set $\zeta_\star\varepsilon_\star = 0.5$ (i.e., half of the stellar envelope exchanges angular momentum), but tidal migration could be slower for smaller $\zeta_\star\varepsilon_\star$, and vice versa. However, such variations are not significant for this system, as they are within the same order of magnitude as presented in Figure 8.

Since $P_{orb} \geqslant \frac{P_{rot\_ini,\star}}{2}$ in all the studied scenarios for $P_{rot\_ini,\star}$ in Figure 8, we only calculate stellar dissipation through the excitation of inertial waves in the convective envelope. In addition, the mass of the planet is not sufficient for wave breaking to occur, and thus internal gravity waves in radiative zones would not be fully damped by tidal forcing (Barker 2020). The results presented here agree with those in Alvarado-Montes (2022), where the orbital evolution of TOI-1899 b induced by stellar tides is also minimum and not significant for

[40] For a more complete description of these parameters and their values, see Dobbs-Dixon et al. (2004) and Alvarado-Montes et al. (2021).

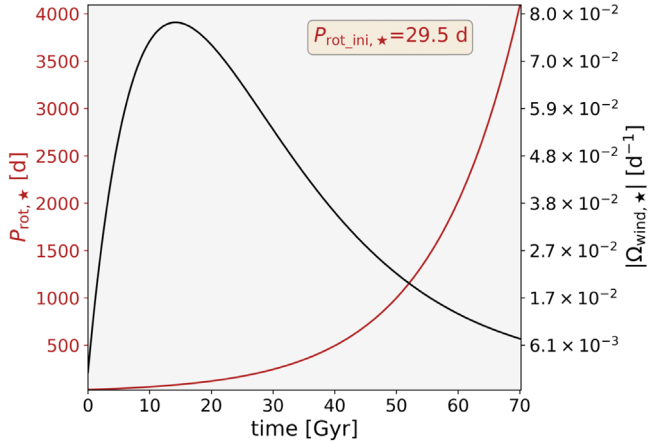

Figure 9. Stellar rotation period (red, left-hand y-axis) and stellar wind braking rate (black, right-hand y-axis), as a function of time. Both quantities were analyzed for a $P_{rot\_ini,\star} \sim 29.5$ days and a star with half of its envelope contributing to the exchange of angular momentum (i.e., $\varepsilon_\star\zeta_\star = 0.5$).

most stellar rotation periods, with migration timescales being generally $\gtrsim$10 Gyr.

6. Conclusion

We have greatly refined the planetary parameters of the M-dwarf WJ TOI-1899 b, using 33 new RVs from the precision spectrographs HPF and NEID and transit photometry from the ground and from three new sectors of TESS. Most notably, we derive a more precise period for this relatively long period planet, $P = 29.090312^{+0.000036}_{-0.000035}$ days, and we find that TOI-1899 b is not as inflated as initially thought, with the original radius (derived from a single TESS transit) being $R_p = 1.15^{+0.04}_{-0.05}\,R_J$ and our joint fit including ground-based data, instead yielding a radius of $0.99 \pm 0.03\,R_J$. We also find that the orbit is less eccentric than previously believed, with the new value of $e = 0.044^{+0.029}_{-0.027}$ consistent with zero at 2σ. The star TOI-1899 is activity quiet over the past 3 yr of RV observations and a slow rotator, with a tentative rotation period $\sim$29.5 days. Among the scarce handful of transiting gas giants orbiting M dwarfs, TOI-1899 b is by far the coolest, with an equilibrium temperature of $T_{eq} \sim 380$ K. With our new ephemeris allowing for extremely precise knowledge of transit times for many years, we encourage transmission spectroscopy studies of this unique planet with JWST, which may offer insights into the formation of gas giants around cool stars.

Acknowledgments

We thank the anonymous referee for valuable feedback, which has improved the quality of this manuscript.

J.A.A.-M. is funded by the International Macquarie University Research Excellence Scholarship ("iMQRES"). C.I.C. acknowledges support by NASA Headquarters through an appointment to the NASA Postdoctoral Program at the Goddard Space Flight Center, administered by USRA through a contract with NASA and the NASA Earth and Space Science Fellowship Program through grant 80NSSC18K1114. G.S. acknowledges support provided by NASA through the NASA Hubble Fellowship grant HST-HF2-51519.001-A awarded by the Space Telescope Science Institute, which is operated by the Association of Universities for Research in Astronomy, Inc., for NASA, under contract NAS5-26555. Part of this research

was carried out at the Jet Propulsion Laboratory, California Institute of Technology, under a contract with the National Aeronautics and Space Administration (80NM0018D0004).

The Center for Exoplanets and Habitable Worlds is supported by Penn State and the Eberly College of Science. Computations for this research were performed on the Pennsylvania State University's Institute for Computational and Data Sciences Advanced CyberInfrastructure (ICDS-ACI), including the CyberLAMP cluster supported by NSF grant MRI-1626251. This content is solely the responsibility of the authors and does not necessarily represent the views of the Institute for Computational and Data Sciences. The Pennsylvania State University campuses are located on the original homelands of the Erie, Haudenosaunee (Seneca, Cayuga, Onondaga, Oneida, Mohawk, and Tuscarora), Lenape (Delaware Nation, Delaware Tribe, Stockbridge-Munsee), Shawnee (Absentee, Eastern, and Oklahoma), Susquehannock, and Wahzhazhe (Osage) Nations. As a land grant institution, we acknowledge and honor the traditional caretakers of these lands and strive to understand and model their responsible stewardship. We also acknowledge the longer history of these lands and our place in that history.

These results are based on observations obtained with the Habitable-zone Planet Finder Spectrograph on the HET. We acknowledge support from NSF grants AST-1006676, AST-1126413, AST-1310885, AST-1310875, AST-1910954, AST-1907622, AST-1909506, ATI 2009889, ATI-2009982, AST-2108512, and AST-2108801 and the NASA Astrobiology Institute (NNA09DA76A) in the pursuit of precision RVs in the NIR. The HPF team also acknowledges support from the Heising-Simons Foundation via grant 2017-0494. The Hobby-Eberly Telescope is a joint project of the University of Texas at Austin, the Pennsylvania State University, Ludwig-Maximilians-Universität München, and Georg-August Universität Gottingen. The HET is named in honor of its principal benefactors, William P. Hobby and Robert E. Eberly. The HET Collaboration acknowledges the support and resources from the Texas Advanced Computing Center. We thank the Resident Astronomers and Telescope Operators at the HET for the skillful execution of our observations with HPF. We would like to acknowledge that the HET is built on Indigenous land. Moreover, we would like to acknowledge and pay our respects to the Carrizo & Comecrudo, Coahuiltecan, Caddo, Tonkawa, Comanche, Lipan Apache, Alabama-Coushatta, Kickapoo, Tigua Pueblo, and all the American Indian and Indigenous Peoples and communities who have been or have become a part of these lands and territories in Texas, here on Turtle Island.

Based on observations at Kitt Peak National Observatory, NSF's NOIRLab, managed by the Association of Universities for Research in Astronomy (AURA) under a cooperative agreement with the National Science Foundation. The authors are honored to be permitted to conduct astronomical research on Iolkam Du'ag (Kitt Peak), a mountain with particular significance to the Tohono O'odham. Deepest gratitude to Zade Arnold, Joe Davis, Michelle Edwards, John Ehret, Tina Juan, Brian Pisarek, Aaron Rowe, Fred Wortman, the Eastern Area Incident Management Team, and all of the firefighters and air support crew who fought the recent Contreras fire. Against great odds, you saved Kitt Peak National Observatory. Data presented herein were obtained at the WIYN Observatory from telescope time allocated to NN-EXPLORE through the scientific partnership of the National Aeronautics and Space Administration, the National Science Foundation, and the National Optical Astronomy Observatory. WIYN is a joint facility of the University of Wisconsin–Madison, Indiana University, NSF's NOIRLab, the Pennsylvania State University, Purdue University, University of California, Irvine, and the University of Missouri. Data presented were obtained by the NEID spectrograph built by Penn State University and operated at the WIYN Observatory by NSF's NOIRLab, under the NN-EXPLORE partnership of the National Aeronautics and Space Administration and the National Science Foundation. This work was performed for the Jet Propulsion Laboratory, California Institute of Technology, sponsored by the United States Government under the Prime Contract 80NM0018D0004 between Caltech and NASA. These results are based on observations obtained with NEID under proposals 2021B-0035 (PI: S. Kanodia) and 2022A-802765 (PI: C. Cañas). We thank the NEID Queue Observers and WIYN Observing Associates for their skillful execution of our NEID observations.

The ground-based photometry is based on observations obtained with the Apache Point Observatory 3.5 m telescope, which is owned and operated by the Astrophysical Research Consortium. We acknowledge support from NSF grants AST 1907622, AST 1909506, AST 1909682, and AST 1910954 and the Research Corporation in connection with precision diffuser-assisted photometry.

Based on observations obtained with the Samuel Oschin 48-inch Telescope at the Palomar Observatory as part of the Zwicky Transient Facility project. ZTF is supported by the National Science Foundation under grant No. AST-1440341 and a collaboration including Caltech, IPAC, the Weizmann Institute for Science, the Oskar Klein Center at Stockholm University, the University of Maryland, the University of Washington, Deutsches Elektronen-Synchrotron and Humboldt University, Los Alamos National Laboratories, the TANGO Consortium of Taiwan, the University of Wisconsin at Milwaukee, and Lawrence Berkeley National Laboratories. Operations are conducted by COO, IPAC, and UW.

This research has made use of the SIMBAD database, operated at CDS, Strasbourg, France, and NASA's Astrophysics Data System Bibliographic Services. This research has made use of the Exoplanet Follow-up Observation Program (ExoFOP; NExScI 2022) website, which is operated by the California Institute of Technology, under contract with the National Aeronautics and Space Administration under the Exoplanet Exploration Program. This research has made use of the NASA Exoplanet Archive, which is operated by Caltech, under contract with NASA under the Exoplanet Exploration Program.

Some of the data presented in this paper were obtained from MAST at STScI. Support for MAST for non-HST data is provided by the NASA Office of Space Science via grant NNX09AF08G and by other grants and contracts. This work includes data collected by the TESS mission, which are publicly available from MAST. The specific observations analyzed can be accessed via DOI:10.17909/SBX7-VG73. Funding for the TESS mission is provided by the NASA Science Mission directorate.

This work presents results from the European Space Agency (ESA) space mission Gaia. Gaia data are being processed by the Gaia Data Processing and Analysis Consortium (DPAC). Funding for the DPAC is provided by national institutions, in particular the institutions participating in the Gaia MultiLateral Agreement (MLA). The Gaia mission website is https://www.cosmos.esa.int/gaia. The Gaia archive website is https://archives.esac.esa.int/gaia.

Facilities: HET (HPF), WIYN 3.5m (NEID), TESS, APO 3.5m (ARCTIC), Gaia.

Software: `AstroImageJ` (Collins et al. 2017), `astropy` (Robitaille et al. 2013; Astropy Collaboration et al. 2018), `barycorrpy` (Kanodia & Wright 2018), `batman` (Kreidberg 2015), `celerite` (Foreman-Mackey et al. 2017; Foreman-Mackey 2018), `dynesty` (Speagle 2020), `EXOFASTv2` (Eastman et al. 2019), `ExoTransmit` (Kempton et al. 2017), `HxRGproc` (Ninan et al. 2018), `ipython` (Pérez & Granger 2007), `juliet` (Espinoza et al. 2019), `matplotlib` (Hunter 2007), `numpy` (Harris et al. 2020), `pandas` (McKinney 2010), `PandExo` (Batalha et al. 2017), `radvel` (Fulton et al. 2018), `scipy` (Virtanen et al. 2020), `SERVAL` (Zechmeister et al. 2018), `TESS-SIP` (Hedges et al. 2020), `tglc` (Han & Brandt 2023), `thejoker` (Price-Whelan et al. 2017).

Appendix A
Lack of Activity Correlation with HPF RVs

As discussed in Section 3.1, we did not find any strong correlations between the HPF RVs and the HPF activity indicators (dLW, CRX, and Ca IRT 1, 2, and 3 indices) using the Kendall rank correlation coefficient (Kendall τ). We show the GLS periodograms in Figure 10, demonstrating that only the planetary RV signal greatly exceeds the false-alarm thresholds, and it is not associated with similarly strong peaks in any of the activity indicators. Figure 11 further shows that, of the activity indicators, only dLW shows any correlation with RVs—but the correlation is weak ($\tau = -0.24$), and the corresponding periodogram peaks are far less significant than the RV signal. The data presented here are available as Data Behind Figures.

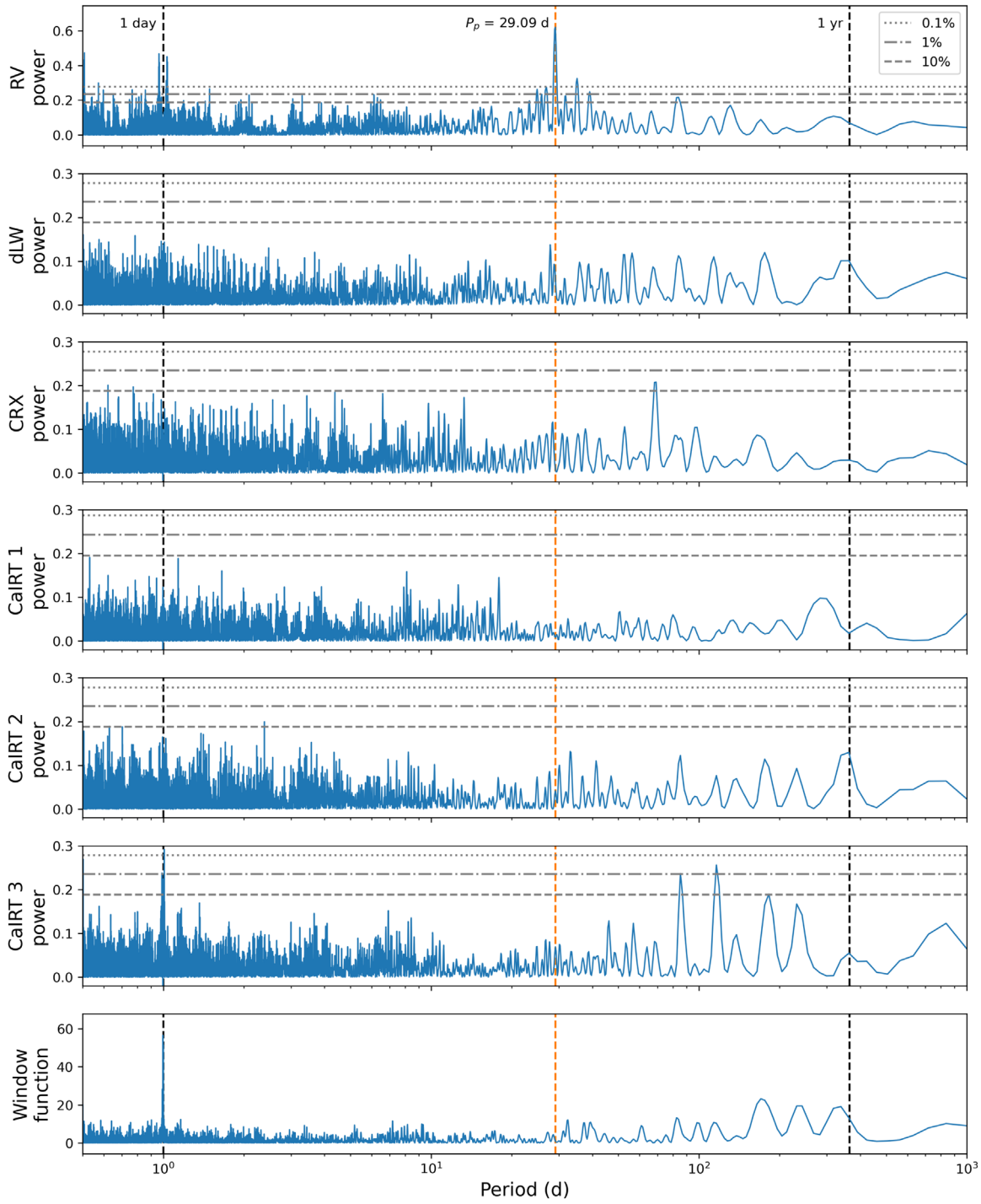

Figure 10. GLS periodograms of the HPF RVs, activity indicators, and window function, with the period of TOI-1899 b indicated by the vertical orange line. The FAP levels corresponding to 0.1%, 1%, and 10% are also marked.

(The data used to create this figure are available.)

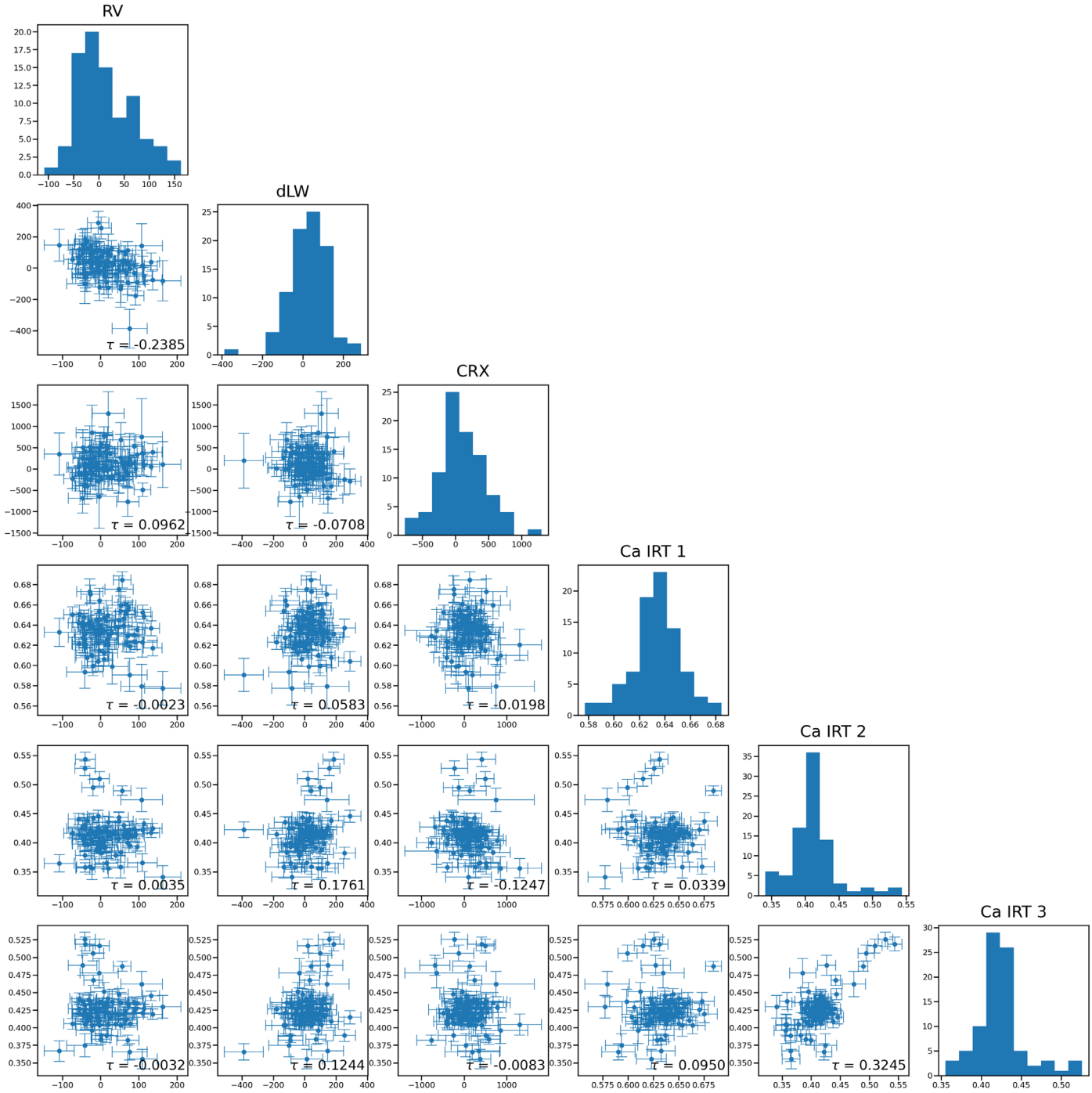

Figure 11. Corner plot of HPF RVs and activity indicators, with the Kendall τ coefficient included for each pair.

Appendix B
Rotationally Modulated Photometric Variability

As discussed in Section 3.2, we examined the publicly available photometry from ASAS-SN in V and g (2015 February 24–2018 November 10 and 2018 April 12–2022 December 22, respectively), ZTF in zr and zg (DR17, which includes data up through 2023 March 9), and TESS (Sectors 14, 15, 41, 54, and 55) in an attempt to determine the rotation period of the host star TOI-1899. We present the GLS periodograms below.

Figure 12 shows that combining the ASAS-SN V and g photometry to form a much longer baseline (see the top panel of Figure 5) boosts the power of the peaks at $P \sim 27$–29 days, which were detected at weak significance when the bands were considered separately. Figure 13 also shows peaks in ZTF zr at $P \sim 31$ days; however, with considerable power in the window function around these periods, aliasing effects are likely at play.

In the TESS photometry (Figure 14), we find that the detected periods in the range of $P \sim 4$–15 days and the relative strengths of the peaks vary greatly from sector to sector—even consecutive sectors, e.g., Sectors 54 and 55. Furthermore, the systematics-insensitive periodogram from `TESS-SIP` (Figure 15) reveals no strong peaks using either the TPFs or the LCFs, with the strongest signals correlated with background periodicity. Taken together, this suggests that the observed photometric variability in PDCSAP cannot be directly measuring the stellar rotation period; it may be an instrumental effect, or may trace some other form of low-level stellar activity.

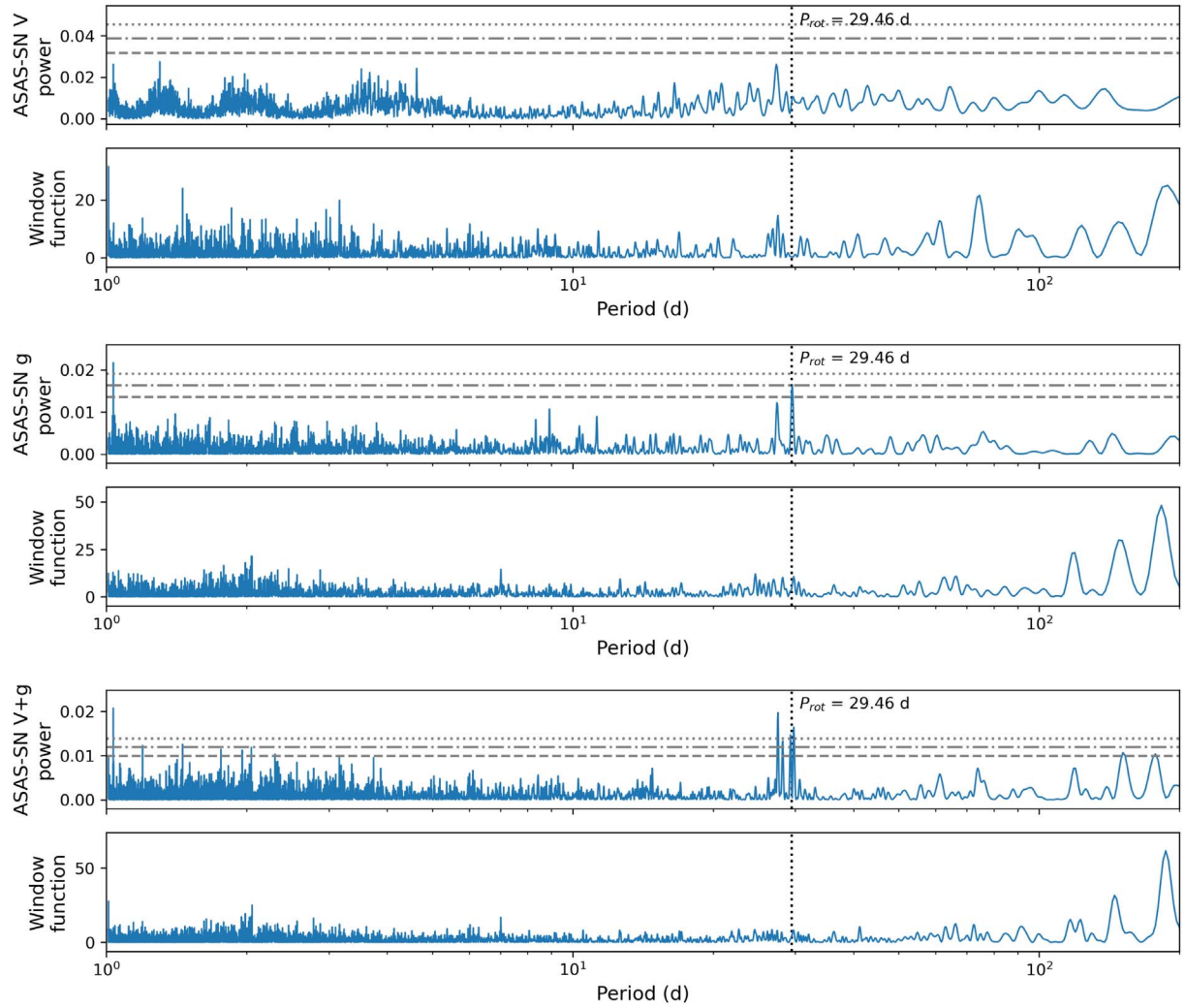

Figure 12. GLS periodograms of available photometry from ASAS-SN (V, g, and combined). We combine V and g in an attempt to more robustly detect long-period signals, since the two bands have little time overlap. FAP levels of 0.1%, 1%, and 10% are marked as in Figure 10, and the tentative rotation period of 29.46 days is shown with a vertical dotted line.

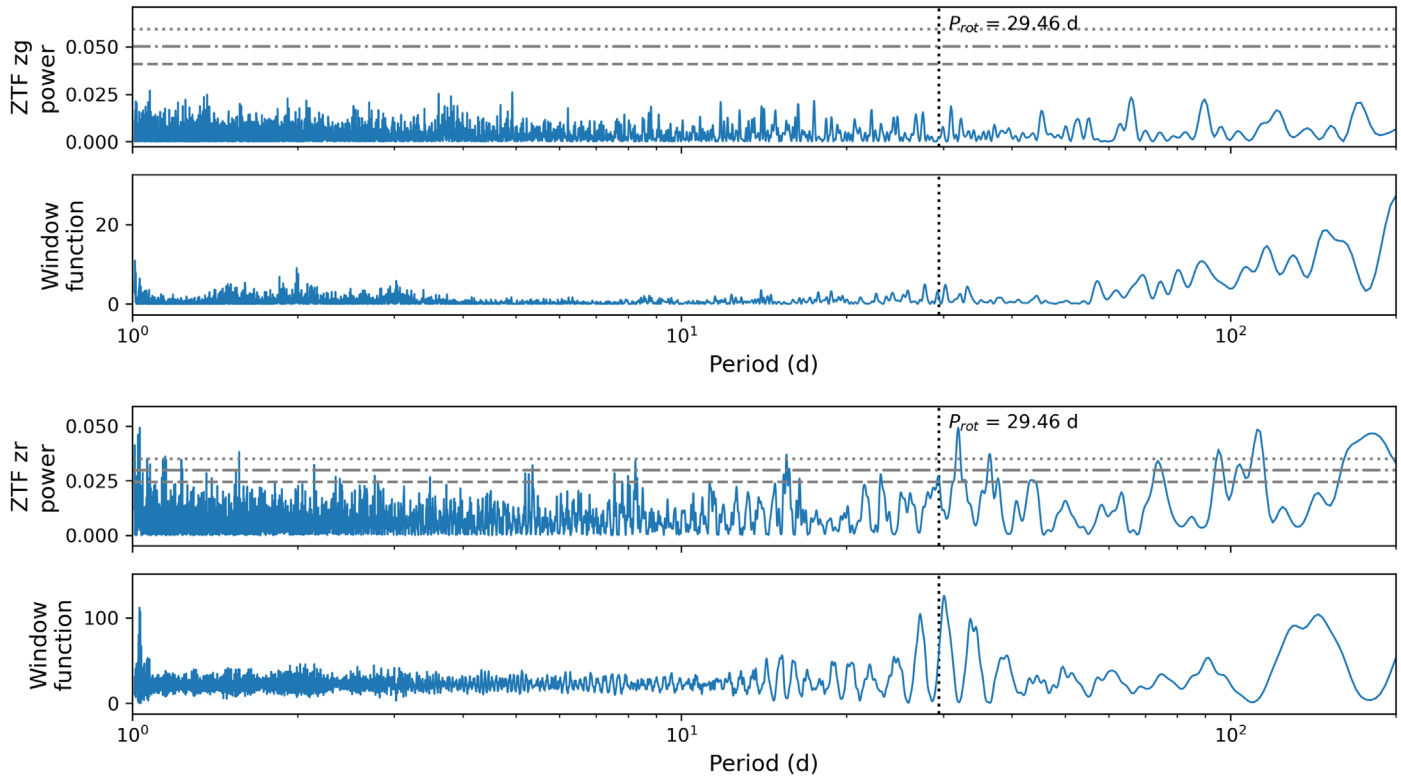

Figure 13. GLS periodograms of available photometry from ZTF (*zg* and *zr*). Here we do not combine the bands as we did with the ASAS-SN data, since the *zg* and *zr* observations span the same time frame.

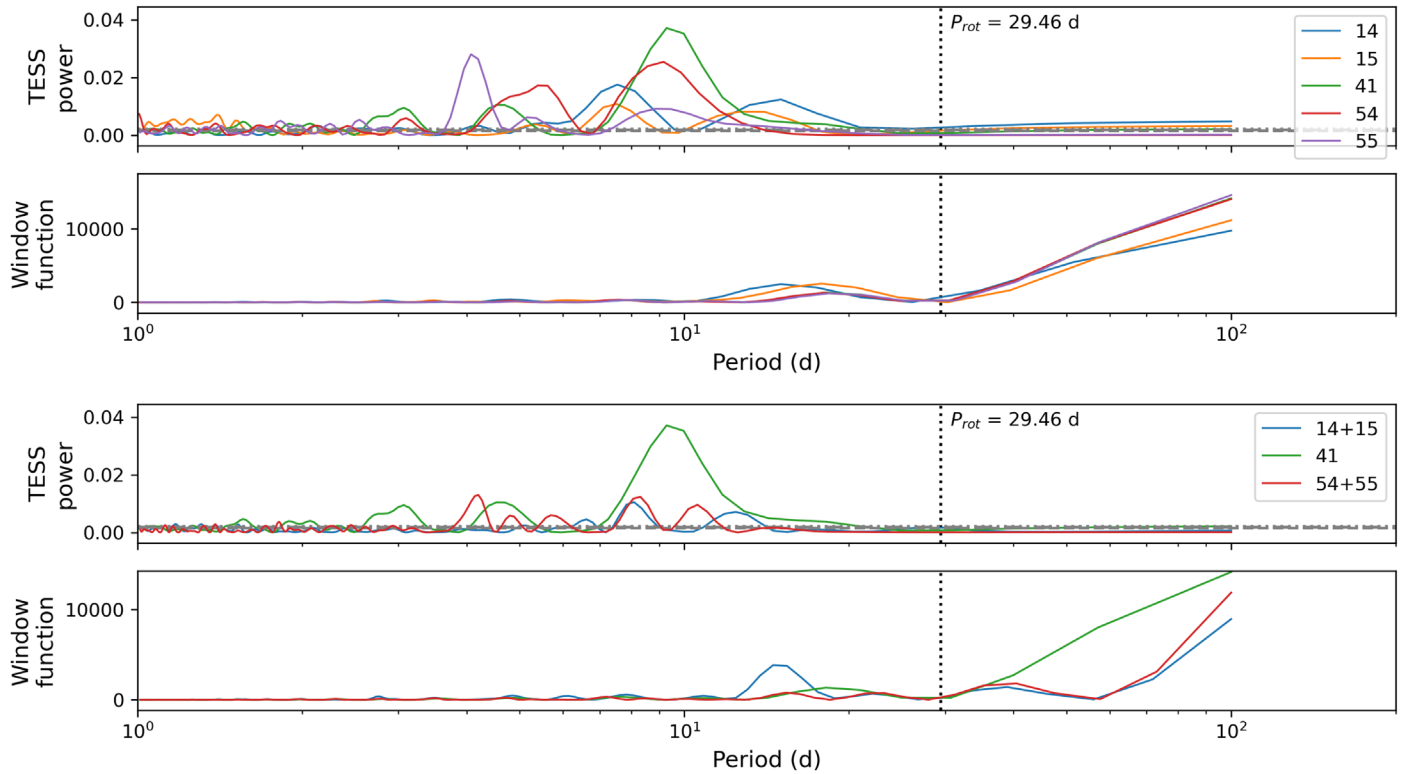

Figure 14. GLS periodograms of available PDCSAP photometry from TESS, with each sector separate (top) and with consecutive sectors grouped together (bottom). The *x*-axis is the same as previous plots for ease of comparison, but smoothing in the PDCSAP processing will suppress any signals $\gtrsim$10 days.

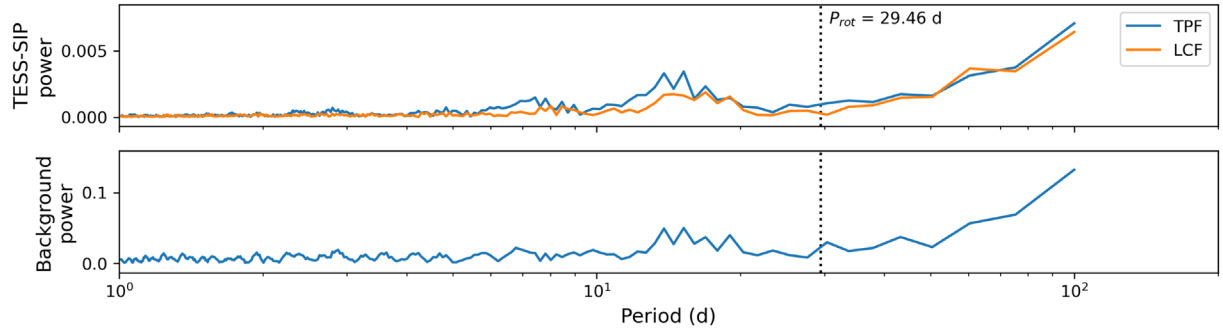

Figure 15. TESS-SIP periodograms computed from both the TPFs and LCFs, neither of which display the periodicity seen in the PDCSAP fluxes.

ORCID iDs

Andrea S. J. Lin https://orcid.org/0000-0002-9082-6337
Jessica E. Libby-Roberts https://orcid.org/0000-0002-2990-7613
Jaime A. Alvarado-Montes https://orcid.org/0000-0003-0353-9741
Caleb I. Cañas https://orcid.org/0000-0003-4835-0619
Shubham Kanodia https://orcid.org/0000-0001-8401-4300
Te Han https://orcid.org/0000-0002-7127-7643
Leslie Hebb https://orcid.org/0000-0003-1263-8637
Eric L. N. Jensen https://orcid.org/0000-0002-4625-7333
Suvrath Mahadevan https://orcid.org/0000-0001-9596-7983
Luke C. Powers https://orcid.org/0000-0002-5300-5353
Tera N. Swaby https://orcid.org/0000-0002-5817-202X
John Wisniewski https://orcid.org/0000-0001-9209-1808
Corey Beard https://orcid.org/0000-0001-7708-2364
Chad F. Bender https://orcid.org/0000-0003-4384-7220
Cullen H. Blake https://orcid.org/0000-0002-6096-1749
William D. Cochran https://orcid.org/0000-0001-9662-3496
Scott A. Diddams https://orcid.org/0000-0002-2144-0764
Robert C. Frazier https://orcid.org/0000-0001-6569-3731
Connor Fredrick https://orcid.org/0000-0002-0560-1433
Michael Gully-Santiago https://orcid.org/0000-0002-4020-3457
Samuel Halverson https://orcid.org/0000-0003-1312-9391
Sarah E. Logsdon https://orcid.org/0000-0002-9632-9382
Michael W. McElwain https://orcid.org/0000-0003-0241-8956
Caroline Morley https://orcid.org/0000-0002-4404-0456
Joe P. Ninan https://orcid.org/0000-0001-8720-5612
Jayadev Rajagopal https://orcid.org/0000-0002-2488-7123
Lawrence W. Ramsey https://orcid.org/0000-0002-4289-7958
Paul Robertson https://orcid.org/0000-0003-0149-9678
Arpita Roy https://orcid.org/0000-0001-8127-5775
Christian Schwab https://orcid.org/0000-0002-4046-987X
Guðmundur Stefánsson https://orcid.org/0000-0001-7409-5688
Daniel J. Stevens https://orcid.org/0000-0002-5951-8328
Ryan C. Terrien https://orcid.org/0000-0002-4788-8858
Jason T. Wright https://orcid.org/0000-0001-6160-5888

References

Allard, F., Homeier, D., & Freytag, B. 2012, RSPTA, 370, 2765
Alvarado-Montes, J. A. 2022, MNRAS, 517, 2831
Alvarado-Montes, J. A., & García-Carmona, C. 2019, MNRAS, 486, 3963
Alvarado-Montes, J. A., Sucerquia, M., García-Carmona, C., et al. 2021, MNRAS, 506, 2247
Andrews, S. M., Rosenfeld, K. A., Kraus, A. L., & Wilner, D. J. 2013, ApJ, 771, 129
Anglada-Escudé, G., & Butler, R. P. 2012, ApJS, 200, 15
Astropy Collaboration, Price-Whelan, A. M., Sipőcz, B. M., et al. 2018, AJ, 156, 123
Bailer-Jones, C. A. L., Rybizki, J., Fouesneau, M., Mantelet, G., & Andrae, R. 2018, AJ, 156, 58
Barclay, T., Kostov, V. B., Colón, K. D., et al. 2021, AJ, 162, 300
Barker, A. J. 2020, MNRAS, 498, 2270
Barker, A. J., & Ogilvie, G. I. 2009, MNRAS, 395, 2268
Batalha, N. E., Lewis, T., Fortney, J. J., et al. 2019, ApJL, 885, L25
Batalha, N. E., Mandell, A., Pontoppidan, K., et al. 2017, PASP, 129, 064501
Brewer, J. M., Fischer, D. A., & Madhusudhan, N. 2017, AJ, 153, 83
Brown, D. J. A., Collier Cameron, A., Hall, C., Hebb, L., & Smalley, B. 2011, MNRAS, 415, 605
Burn, R., Schlecker, M., Mordasini, C., et al. 2021, A&A, 656, A72
Burt, J. A., Nielsen, L. D., Quinn, S. N., et al. 2020, AJ, 160, 153
Cañas, C. I., Kanodia, S., Bender, C. F., et al. 2022, AJ, 164, 50
Cañas, C. I., Stefansson, G., Kanodia, S., et al. 2020, AJ, 160, 147
Chambers, K. C., Magnier, E. A., Metcalfe, N., et al. 2016, arXiv:1612.05560
Choi, J., Dotter, A., Conroy, C., et al. 2016, ApJ, 823, 102
Christiansen, J. L., Bhure, S., Zink, J. K., et al. 2022, AJ, 163, 244
Claytor, Z. R., van Saders, J. L., Llama, J., et al. 2022, ApJ, 927, 219
Clough, S. A., Shephard, M. W., Mlawer, E. J., et al. 2005, JQSRT, 91, 233
Collins, K. A., Kielkopf, J. F., Stassun, K. G., & Hessman, F. V. 2017, AJ, 153, 77
Cutri, R. M., Skrutskie, M. F., van Dyk, S., et al. 2003, yCat, II/246
Dawson, R. I., & Johnson, J. A. 2018, ARA&A, 56, 175
Dobbs-Dixon, I., Lin, D. N. C., & Mardling, R. A. 2004, ApJ, 610, 464
Dotter, A. 2016, ApJS, 222, 8
Dymont, A. H., Yu, X., Ohno, K., Zhang, X., & Fortney, J. J. 2022, ApJ, 937, 90
Eastman, J. 2017, EXOFASTv2: Generalized publication-quality exoplanet modeling code, Astrophysics Source Code Library, ascl:1710.003
Eastman, J. D., Rodriguez, J. E., Agol, E., et al. 2019, arXiv:1907.09480
Espinoza, N., Kossakowski, D., & Brahm, R. 2019, MNRAS, 490, 2262
Foreman-Mackey, D. 2018, RNAAS, 2, 31
Foreman-Mackey, D., Agol, E., Ambikasaran, S., & Angus, R. 2017, AJ, 154, 220
Fortney, J. J., Marley, M. S., & Barnes, J. W. 2007, ApJ, 659, 1661
Fortney, J. J., Visscher, C., Marley, M. S., et al. 2020, AJ, 160, 288
Fulton, B. J., Petigura, E. A., Blunt, S., & Sinukoff, E. 2018, PASP, 130, 044504
Gaia Collaboration, Vallenari, A., Brown, A. G. A., et al. 2023, A&A, 674, A1
Gallet, F., Bolmont, E., Mathis, S., Charbonnel, C., & Amard, L. 2017, A&A, 604, A112
Gan, T., Lin, Z., Wang, S. X., et al. 2022, MNRAS, 511, 83
Green, G. M., Schlafly, E., Zucker, C., Speagle, J. S., & Finkbeiner, D. 2019, ApJ, 887, 93
Guenel, M., Mathis, S., & Remus, F. 2014, A&A, 566, L9
Guillochon, J., Ramirez-Ruiz, E., & Lin, D. 2011, ApJ, 732, 74
Gullikson, K., Dodson-Robinson, S., & Kraus, A. 2014, AJ, 148, 53
Halverson, S., Terrien, R., Mahadevan, S., et al. 2016, Proc. SPIE, 9908, 99086P
Han, T., & Brandt, T. D. 2023, AJ, 165, 71
Harris, C. R., Millman, K. J., van der Walt, S. J., et al. 2020, Natur, 585, 357
Hedges, C., Angus, R., Barentsen, G., et al. 2020, RNAAS, 4, 220

Henden, A. A., Levine, S., Terrell, D., & Welch, D. L. 2015, AAS Meeting Abstracts, 225, 336
Hill, G. J., Lee, H., MacQueen, P. J., et al. 2021, AJ, 162, 298
Huang, C., Wu, Y., & Triaud, A. H. M. J. 2016, ApJ, 825, 98
Huehnerhoff, J., Ketzeback, W., Bradley, A., et al. 2016, Proc. SPIE, 9908, 99085H
Hunter, J. D. 2007, CSE, 9, 90
Ida, S., & Lin, D. N. C. 2004, ApJ, 604, 388
Jenkins, J. M., Twicken, J. D., McCauliff, S., et al. 2016, Proc. SPIE, 9913, 99133E
Kanodia, S., Mahadevan, S., Ramsey, L. W., et al. 2018, Proc. SPIE, 10702, 107026Q
Kanodia, S., & Wright, J. 2018, RNAAS, 2, 4
Kasper, D. H., Ellis, T. G., Yeigh, R. R., et al. 2016, PASP, 128, 105005
Kempton, E. M. R., Bean, J. L., Louie, D. R., et al. 2018, PASP, 130, 114401
Kempton, E. M. R., Lupu, R., Owusu-Asare, A., Slough, P., & Cale, B. 2017, PASP, 129, 044402
Kipping, D. M. 2013, MNRAS, 435, 2152
Kochanek, C. S., Shappee, B. J., Stanek, K. Z., et al. 2017, PASP, 129, 104502
Kreidberg, L. 2015, PASP, 127, 1161
Lainey, V., Arlot, J.-E., Karatekin, Ö., & van Hoolst, T. 2009, Natur, 459, 957
Laughlin, G., Bodenheimer, P., & Adams, F. C. 2004, ApJL, 612, L73
Leconte, J., Wu, H., Menou, K., & Murray, N. 2015, Sci, 347, 632
Libby-Roberts, J. E., Berta-Thompson, Z. K., Diamond-Lowe, H., et al. 2022, AJ, 164, 59
Logsdon, S. E., McElwain, M. W., Gong, Q., et al. 2018, Proc. SPIE, 10702, 1070267
Madhusudhan, N. 2018, in Handbook of Exoplanets, ed. H. J. Deeg & J. A. Belmonte (London: Springer), 104
Mahadevan, S., Ramsey, L., Bender, C., et al. 2012, Proc. SPIE, 8446, 84461S
Mahadevan, S., Ramsey, L. W., Terrien, R., et al. 2014, Proc. SPIE, 9147, 91471G
Maldonado, J., Micela, G., Baratella, M., et al. 2020, A&A, 644, A68
Mandel, K., & Agol, E. 2002, ApJL, 580, L171
Mann, A. W., Wood, M. L., Schmidt, S. P., et al. 2022, AJ, 163, 156
Masci, F. J., Laher, R. R., Rusholme, B., et al. 2019, PASP, 131, 018003
Mathis, S. 2015, in SF2A-2015: Proc.of the Annual meeting of the French Society of Astronomy and Astrophysics, ed. F. Martins et al. (Toulouse: SF2A), 283
Matsumura, S., Peale, S. J., & Rasio, F. A. 2010, ApJ, 725, 1995
McCormac, J., Gillen, E., Jackman, J. A. G., et al. 2019, arXiv:1909.12424
McKinney, W. 2010, in Proc. of the IX Python in Science Conf., ed. S. van der Walt & J. Millman (Austin, TX: SciPy), 56
Metcalf, A., Anderson, T., Bender, C., et al. 2019, Optica, 6, 233
Morton, T. D., Bryson, S. T., Coughlin, J. L., et al. 2016, ApJ, 822, 86
Müller, S., & Helled, R. 2023, A&A, 669, A24
2020, Planetary Systems Composite TableNASA Exoplanet Science Institute, IPAC, doi:10.26133/NEA13
NExScI 2022, Exoplanet Follow-up Observing Program Web Service, IPAC, doi:10.26134/EXOFOP5
Ninan, J. P., Bender, C. F., Mahadevan, S., et al. 2018, Proc. SPIE, 10709, 107092U
Öberg, K. I., Murray-Clay, R., & Bergin, E. A. 2011, ApJL, 743, L16
Ogilvie, G. I. 2013, MNRAS, 429, 613
Panahi, A., Zucker, S., Clementini, G., et al. 2022, A&A, 663, A101
Perez, F., & Granger, B. E. 2007, CSE, 9, 21
Price-Whelan, A. M., Hogg, D. W., Foreman-Mackey, D., & Rix, H.-W. 2017, ApJ, 837, 20
Rackham, B. V., Apai, D., & Giampapa, M. S. 2018, ApJ, 853, 122
Ramsey, L. W., Adams, M. T., Barnes, T. G., et al. 1998, Proc. SPIE, 3352, 34
Ricker, G. R., Winn, J. N., Vanderspek, R., et al. 2014, Proc. SPIE, 9143, 914320
Robertson, P., Anderson, T., Stefansson, G., et al. 2019, JATIS, 5, 015003
Robichon, N., & Arenou, F. 2000, A&A, 355, 295
Robitaille, T. P., Tollerud, E. J., Greenfield, P., et al. 2013, A&A, 558, A33
Roche, E. 1849, Acad. Montpellier, 1, 243
Rodríguez, A., & Ferraz-Mello, S. 2010, EAS, 42, 411
Schwab, C., Liang, M., Gong, Q., et al. 2018, Proc. SPIE, 10702, 1070271
Schwab, C., Rakich, A., Gong, Q., et al. 2016, Proc. SPIE, 9908, 99087H
Shetrone, M., Cornell, M. E., Fowler, J. R., et al. 2007, PASP, 119, 556
Speagle, J. S. 2020, MNRAS, 493, 3132
Stefansson, G., Cañas, C., Wisniewski, J., et al. 2020, AJ, 159, 100
Stefansson, G., Hearty, F., Robertson, P., et al. 2016, ApJ, 833, 175
Stefansson, G., Li, Y., Mahadevan, S., et al. 2018a, AJ, 156, 266
Stefansson, G., Mahadevan, S., Hebb, L., et al. 2017, ApJ, 848, 9
Stefánsson, G., Mahadevan, S., Petrovich, C., et al. 2022, ApJL, 931, L15
Stefansson, G., Mahadevan, S., Wisniewski, J., et al. 2018b, Proc. SPIE, 10702, 1070250
Tran, Q. H., Bowler, B. P., Endl, M., et al. 2022, AJ, 163, 225
Tsai, S.-M., Lyons, J. R., Grosheintz, L., et al. 2017, ApJS, 228, 20
Virtanen, P., Gommers, R., Oliphant, T. E., et al. 2020, NatMe, 17, 261
Weiss, L. M., Marcy, G. W., Rowe, J. F., et al. 2013, ApJ, 768, 14
Wong, I., Knutson, H. A., Kataria, T., et al. 2016, ApJ, 823, 122
Wright, E. L., Eisenhardt, P. R. M., Mainzer, A. K., et al. 2010, AJ, 140, 1868
Wright, J. T., & Eastman, J. D. 2014, PASP, 126, 838
Yee, S. W., Petigura, E. A., & von Braun, K. 2017, ApJ, 836, 77
Zechmeister, M., Reiners, A., Amado, P. J., et al. 2018, A&A, 609, A12